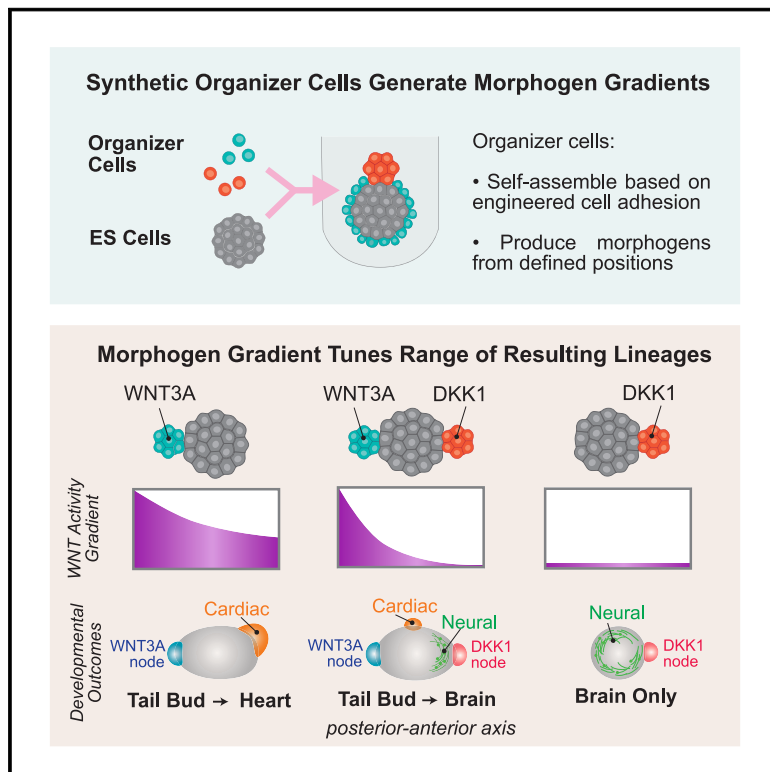


# Synthetic organizer cells guide development via spatial and biochemical instructions

## Graphical abstract



## Authors

Toshimichi Yamada, Coralie Trentesaux, Jonathan M. Brunger, ..., Dario Boffelli, Ophir D. Klein, Wendell A. Lim

## Correspondence

ophir.klein@cshs.org (O.D.K.), wendell.lim@ucsf.edu (W.A.L.)

## In brief

Synthetic organizer cells, engineered to spatially self-assemble around stem cells, can be used to create specific morphogen gradients and systematically guide *in vitro* development.

## Highlights

- Synthetic organizer cells self-assemble around stem cells and produce morphogens
- Induction of WNT3A/DKK1 from different organizer architectures yields diverse gradients
- Full-range WNT gradient yields embryoid with broad anterior-to-posterior lineages
- Shallower WNT gradients yield more complex morphogenesis, e.g., beating cardiac chamber

Article

# Synthetic organizer cells guide development via spatial and biochemical instructions

Toshimichi Yamada,<sup>1,7</sup> Coralie Trentesaux,<sup>2,7</sup> Jonathan M. Brunger,<sup>1,8</sup> Yini Xiao,<sup>1</sup> Adam J. Stevens,<sup>1</sup> Iain Martyn,<sup>1</sup> Petr Kasperek,<sup>2</sup> Neha P. Shroff,<sup>2</sup> Angelica Aguilar,<sup>1</sup> Benoit G. Bruneau,<sup>3,4,5</sup> Dario Boffelli,<sup>6</sup> Ophir D. Klein,<sup>2,4,6,\*</sup> and Wendell A. Lim<sup>1,9,\*</sup>

<sup>1</sup>Cell Design Institute and Department of Cellular and Molecular Pharmacology, University of California, San Francisco, San Francisco, CA 94158, USA

<sup>2</sup>Department of Orofacial Sciences and Program in Craniofacial Biology, University of California, San Francisco, San Francisco, CA 94143, USA

<sup>3</sup>Gladstone Institutes, San Francisco, CA 94158, USA

<sup>4</sup>Department of Pediatrics, University of California, San Francisco, San Francisco, CA 94143, USA

<sup>5</sup>Cardiovascular Research Institute, University of California, San Francisco, San Francisco, CA 94158, USA

<sup>6</sup>Department of Pediatrics, Cedars-Sinai Guerin Children's, Los Angeles, CA 90048, USA

<sup>7</sup>These authors contributed equally

<sup>8</sup>Present address: Department of Biomedical Engineering, Vanderbilt University, Nashville, TN 37212, USA

<sup>9</sup>Lead contact

\*Correspondence: [ophir.klein@cshs.org](mailto:ophir.klein@cshs.org) (O.D.K.), [wendell.lim@ucsf.edu](mailto:wendell.lim@ucsf.edu) (W.A.L.)

<https://doi.org/10.1016/j.cell.2024.11.017>

## SUMMARY

*In vitro* development relies primarily on treating progenitor cells with media-borne morphogens and thus lacks native-like spatial information. Here, we engineer morphogen-secreting organizer cells programmed to self-assemble, via cell adhesion, around mouse embryonic stem (ES) cells in defined architectures. By inducing the morphogen WNT3A and its antagonist DKK1 from organizer cells, we generated diverse morphogen gradients, varying in range and steepness. These gradients were strongly correlated with morphogenetic outcomes: the range of minimum-maximum WNT activity determined the resulting range of anterior-to-posterior (A-P) axis cell lineages. Strikingly, shallow WNT activity gradients, despite showing truncated A-P lineages, yielded higher-resolution tissue morphologies, such as a beating, chambered cardiac-like structure associated with an endothelial network. Thus, synthetic organizer cells, which integrate spatial, temporal, and biochemical information, provide a powerful way to systematically and flexibly direct the development of ES or other progenitor cells in different directions within the morphogenetic landscape.

## INTRODUCTION

Over the past decade, remarkable progress has been made in directing the differentiation of pluripotent cells *in vitro*. However, such *in vitro* development has relied primarily on diffuse, media-borne morphogens and thus lacks the complex spatial instructions presented within the native context. Thus, *in vitro* development still lacks the complexity, precision, and reproducibility of native embryogenesis.<sup>1,2</sup> A key missing feature is spatially asymmetric signals encoded within developmental niches. *In vivo* environments often contain signaling centers, such as the Spemann-Mangold organizer,<sup>3</sup> defined as groups of cells present at a specific location in the developing embryo that produce instructive morphogen gradients, guiding the development of neighboring cells (Figure 1A).<sup>4</sup> These graded concentrations of morphogens lead to complex patterns of cell fates and organogenesis.<sup>5</sup> By contrast, common *in vitro* differentiation protocols provide isotropic morphogens in the media,

lacking such spatial information (Figure 1A). Microdevices, beads, transplantation, and optogenetic induction systems provide ways to spatially control signals,<sup>6–10</sup> but these often require precise user manipulation and can come at a cost of decreased ease, throughput, and reproducibility.

Recent studies have shown that extra-embryonic cells from trophoblasts or primitive endoderm can act as organizers/signaling centers for *in vitro* embryos. The extra-embryonic cells self-organize around stem cells via specific adhesion interactions and provide spatial instructions, promoting native-like development (Figure 1A).<sup>11,12</sup> Building on more than a century of developmental studies, these advances support a simple hypothesis: we may be able to more systematically guide development *in vitro* if we can engineer synthetic organizer cells that spatially self-assemble around progenitor cells and provide them with spatially defined biochemical signals (Figure 1A).

Here, we demonstrate the ability to program a fibroblast cell line to form “synthetic organizer” cells. We use a toolkit of native

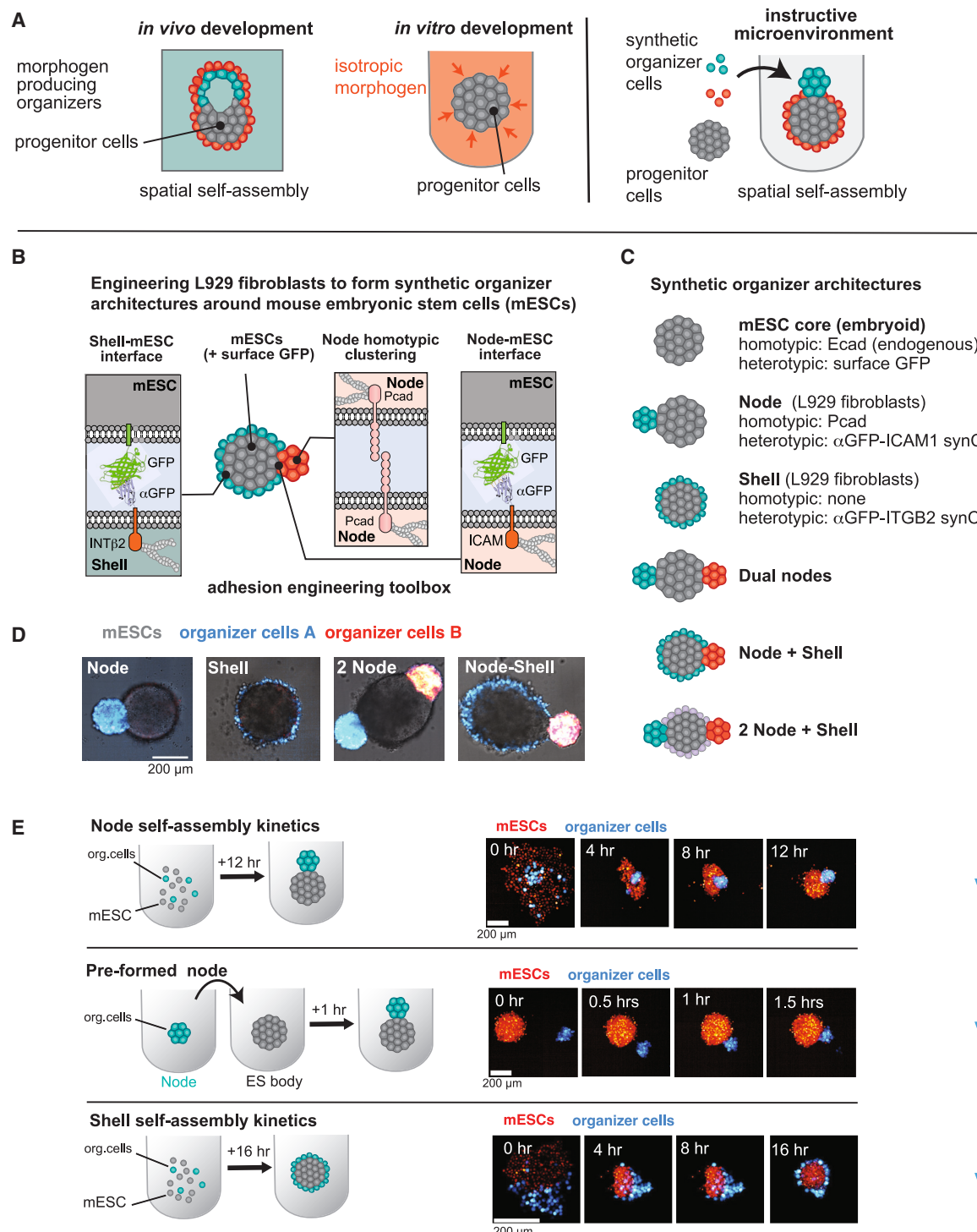


**Figure 1. Programming synthetic organizer architectures to spatially guide development**

(A) Concept of self-assembling synthetic organizer cells to guide *in vitro* development. Endogenous development (left) takes place within complex microenvironments with spatially precise morphogen signals to drive robust and complex development. By contrast, most *in vitro* protocols (center) rely on systemic morphogen stimulation that lacks spatial information. Here, we create synthetic organizer cells (red/blue) programmed to self-assemble around the progenitor cells (gray), providing spatially directed morphogen signals to drive more reliable and complex morphogenesis.

(legend continued on next page)

and synthetic cell adhesion molecules (synCAMs<sup>13</sup>) to engineer cells that self-assemble around mouse embryonic stem cells (mESCs) in customizable architectures. We then harness these architectures to express instructive morphogen signals in specific, spatially asymmetric patterns, controlled by small molecule inducers. Expressing the morphogen Wingless-related integration site 3 A (WNT3A) and its antagonist Dickkopf-1 (DKK1) in different organizer architectures generates a set of systematically varied morphogen activity gradients, allowing us to explore how subtle changes in the gradient guide the embryo toward distinct outcomes. We find that a wide dynamic range of maximum-to-minimum Wnt activity induces a comprehensive progression of anterior-to-posterior (A-P) cell lineages. By contrast, shallow gradients with a smaller dynamic range, while resulting in a truncated range of A-P lineages, can induce spontaneous formation of highly organized tissues, such as a beating cardiac chamber associated with an extensive endothelial network. Thus, synthetic organizer cells, which combine adhesion-based assembly with biochemical signaling, provide a powerful way to systematically encode positional information to guide development *in vitro*.

## RESULTS

### Programming distinct synthetic organizer cell architectures using engineered cell adhesion

Here, we define a synthetic organizer as a group of morphogen-producing cells engineered to self-assemble around progenitor cells (mESCs) in a spatially defined manner—they provide morphogen signals from a defined spatial position. To program different synthetic organizer architectures, we harnessed the differential adhesion hypothesis,<sup>14</sup> which postulates that multicellular systems self-assemble into a minimal energy structure based on the relative strengths of cell adhesion interactions. We have recently developed a toolkit of natural and synthetic adhesion molecules that can be used to tune both the specificity and strength of homotypic and heterotypic adhesion, allowing one to program self-assembly of engineered multicellular systems.<sup>13</sup> Here, we used this adhesion toolkit to engineer a simple L929 fibroblast cell line to self-assemble around mESCs in a user-defined manner (Figures 1B and 1C). To facilitate this, we created an mESC line expressing non-fluorescent GFP on its surface using PiggyBac transposon system. The surface GFP could then be recognized by synCAMs with anti-GFP nanobodies.<sup>15</sup>

We postulated that L929 cell variants could form either “node” or “shell” organizer architectures by introducing adhesion molecules with lentiviral transduction (Figures 1B and 1C). In this context, a node architecture is a cluster of organizer cells inter-

acting with the embryo at a single point, while a shell architecture is a single layer of organizer cells surrounding the embryo. A node would provide a localized source of morphogen, with a shell providing a spherically uniform morphogen source.

To make a node architecture, we first tested L929 cells expressing the natural homophilic cadherins, N, K, or P cadherin (PCAD), and found that PCAD yielded the best segregation from E-cadherin-expressing mESCs (Figure S1B). We then tethered the node to the embryo by expressing an anti-GFP synCAM in the L929 cells (mESCs express surface non-fluorescent GFP ligand). We found that a synCAM with the intracellular domain from Intercellular adhesion molecule-1 (ICAM-1) yielded a stable, well-formed mESC-tethered node (Figures 1B and S1B). When mESCs and the node cells were mixed, the engineered adhesion led to self-organization into a single-node attached to the embryo (Figures 1D and 1E; Video S1). Further, we found that node formation was 5–10 times faster and more consistent (fewer multi-node structures) if we preformed the node and mESC clusters separately and then mixed them (Figures 1E and S1C; Video S1). By independently pre-forming two separate nodes and mixing them with an embryo, we could also reliably (~50%) generate structures with two different nodes (Figure S1D).

To create a shell architecture, we screened anti-GFP synCAMs and found that those with the integrin β1 (ITGB1) or integrin β2 (ITGB2) intracellular domains consistently yielded single-layer shells around the GFP+ embryo (Figure S1B). Mixing these shell L929 cells with GFP+ mESCs led to self-organization of a shell architecture (Figures 1D and 1E; Video S1). By using multiple L929 organizer cell lines, we could now program structures with combinations of one or two nodes and a shell.

When building structures with two nodes, we found that the angular separation could vary (Figure S1E). Notably, however, when we tracked such assemblies over several days, nodes attached with the ICAM-1 synCAM showed significantly less angular change compared with nodes only expressing PCAD (Figure S1F). This result suggests that strong adhesion can lock the nodes into more fixed positions on the embryo surface. This stability is important, as movement of nodes along the embryo’s surface might otherwise blur the positional information encoded in the gradients.

### Synthetic organizers provide spatiotemporal control of morphogen signaling

We next sought to use our synthetic organizer cells to provide morphogen signals. Here, we focused on WNT3A, which plays a central role in early embryogenesis, and its secreted antagonist DKK1, with the overall goal of using both agonist and antagonist in a coordinated way to reshape morphogenetic signaling. We

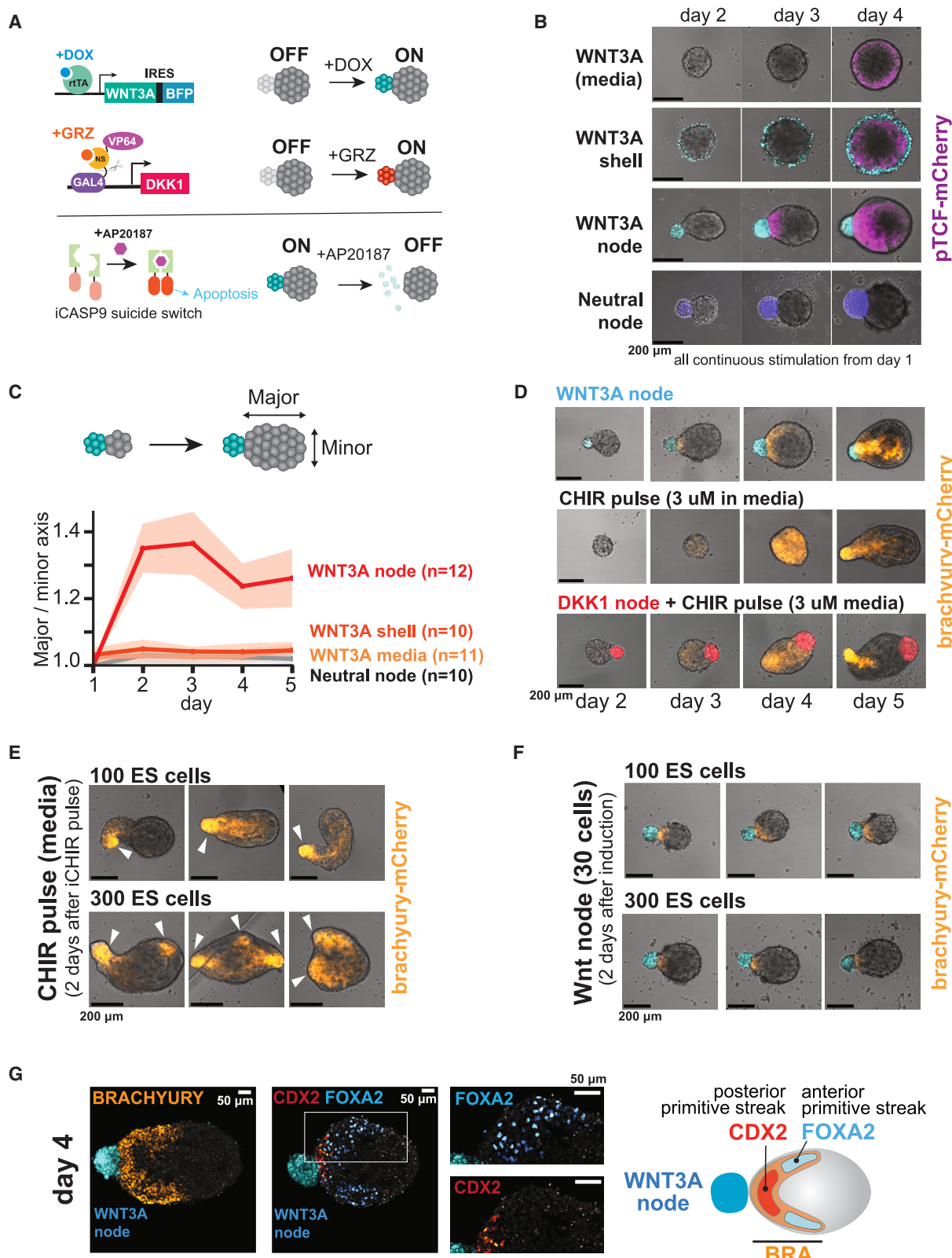
(B) Cell adhesion engineering toolbox to build synthetic organizer architectures of L929 fibroblasts (red/blue) around mESCs (gray). mESCs express surface nfGFP ligand. L929 cells expressing anti-GFP synCAM with integrin β2 (ITGB2) intracellular domain (blue) form a shell, while L929 cells expressing PCAD and anti-GFP synCAM with ICAM intracellular domain form a node anchored to the mESCs embryo.

(C) Combinatorial synthetic organizer architectures built from shell and node organizer cells.

(D) Bright-field images exemplifying synthetic organizer architectures (blue or red L929 cells) around a mESC embryo. Scale bar: 200 μm.

(E) Live imaging of organizer self-assembly. Node cells (blue) self-organize with mESCs (red) in ~12 h (middle, Video S1). Preformed organizer node leads to more rapid and reliable assembly (right, Video S1). Shell self-assembly kinetics (left, Video S1). Scale bar: 200 μm.

See Figure S1 for a more complete analysis of self-assembly properties of L929 organizer cells expressing a broader range of synCAMs.



(legend on next page)

could directly monitor WNT pathway activation in the mESCs by using a WNT reporter mESC line (pTCF-mCherry).<sup>16,17</sup>

To dynamically control morphogen production, we engineered organizer cells with small molecule-inducible promoters (Figure 2A). WNT3A (with IRES-BFP fusion) was expressed from pTRE (Tet<sub>on</sub> promoter), activated by doxycycline (DOX).<sup>18</sup> DKK1 was expressed from a pGAL4-UAS promoter, induced by grazoprevir (GRZ; drug inhibits proteolysis of GAL4-VP64 transactivator).<sup>19–21</sup> These two systems enabled us to independently control the timing and amplitude of WNT3A and DKK1 production (Figures S2C, S2E, and S4A).

To stop morphogen secretion, we initially explored washing out the inducer molecules, but we found this to be a slow process. Thus, to more precisely halt morphogen secretion, we engineered organizer cells with an inducible suicide switch based on iCasp9 that enables rapid triggering of apoptosis by adding the drug AP20187 (Figures 2A and S2D).<sup>22</sup> When we expose a WNT3 node expressing the suicide switch to AP20187, we observed dissociation of the node cells and loss of BFP reporter expression within a day. Together, these findings show that synthetic organizer cells can serve as a modular system to coordinate biochemical morphogen signaling with both spatial and temporal control.

### Synthetic node organizers can drive mESC symmetry breaking

WNT3A plays a central role in elongation and symmetry breaking during mammalian gastrulation.<sup>23–25</sup> Here, we wanted to provide WNT3A from different spatial sources and determine which were sufficient to break symmetry within an embryoid. We therefore provided continuous WNT3A from (1) the media, (2) a synthetic organizer node, or (3) a synthetic organizer shell (Figures 2A and 2B). As a control, we also examined a neutral organizer node that does not express WNT3A.

By tracking the development of embryoids over the course of 4 days (Figure 2B), we observed that only the WNT3A node broke symmetry, showing asymmetric pTCF reporter activation and distinctive embryoid elongation along the WNT gradient axis (Figures 2B and 2C). Embryoids stimulated by media- and shell-based WNT3A showed radially symmetric pTCF activation

without elongation. A neutral node did not induce any pTCF response or elongation (Figures 2B and S2A), consistent with RNA profiling showing that the L929 cells did not basally produce WNT3A or DKK1 (Figure S2B). Thus, provision of WNT3A from an asymmetric source was sufficient to break symmetry and generate embryoid elongation. Elimination of the WNT3A node with the suicide switch at different time points indicated that at least 3 days of continuous signaling are required to stably induce symmetry breaking (Figure S3A).

To follow subsequent steps in embryoid symmetry breaking, we used an mESC line with a reporter for Brachyury, a canonical early marker of the primitive streak that normally arises at the posterior end of the embryo.<sup>26,27</sup> We found that the WNT3A node induced Brachyury+ cells adjacent to the node by day 3, and those Brachyury-positive cells spread inside the embryoid by day 5, reflecting an extension of the primitive streak (Figure 2D). Importantly, the initial expression of Brachyury consistently occurred adjacent to the WNT3A node, where WNT activity is the highest (no Brachyury induction is observed with a neutral node, Figure S2A). Thus, the WNT3A node organizer appears capable of determining the posterior side of the embryo.

Similar WNT-driven symmetry breaking *in vitro* has been described in the gastruloid models.<sup>26</sup> In this model, however, WNT is not provided from an asymmetric source. Rather, WNT activity is induced through a short pulse of the WNT agonist CHIR99021 (CHIR) between days 2 and 3 (Figure S3B). This pulse initially resulted in uniform Brachyury expression on day 3 (Figure 2D), which then became polarized by day 5. By contrast, the dynamics of symmetry breaking in WNT3A-node embryoids differ significantly, as Brachyury expression is localized and asymmetric from its initial appearance.

While the gastruloid protocol does not require spatial regulation of WNT signaling, it does require a specific pulse time of CHIR as well as specific numbers of ESCs. We therefore compared the robustness of symmetry breaking between gastruloids and node-induced embryoids by varying the initial number of ESCs. While the gastruloid protocol led to a single Brachyury+ pole when seeding 100–200 ESCs, higher cell numbers led to multiple Brachyury+ poles (300 ESCs) or loss of polarization (400 ESCs) (Figures 2E and S3C). By contrast,

### Figure 2. Local node organizers generate morphogen gradients and symmetry breaking

- (A) Genetic circuits that enable temporal and amplitude control of morphogen induction from synthetic organizer cells. WNT3A is induced by doxycycline (DOX), DKK1 by grazoprevir (GRZ), and iCasp9-based suicide switch by AP20187. The bottom shows the timeline of organizer-induced morphogen production used in this study.
- (B) Time-lapse images of representative pTCF-mCherry signal (magenta; WNT activity reporter) in each condition. Initial seeding: 300 mESCs, 30 organizer cells for WNT3A shell or node (or 30 cells for neutral node making no morphogen). On day 1, WNT3A is induced with 200 ng/mL DOX. For WNT3A in media, 160 ng/mL was used. Scale bar: 200  $\mu$ m.
- (C) Quantification of embryoid elongation over time for each condition. Shaded area shows SD from multiple experiments. Scale bar: 200  $\mu$ m.
- (D) Representative time-lapse images of Brachyury-mCherry reporter (orange) in each condition. Scale bar: 200  $\mu$ m. Initial seeding: 200 SBR ESCs, 30 organizer cells for WNT3A node and DKK1 node. WNT3A (continuous) is induced on day 1 by adding 200 ng/mL DOX. Gastruloid generation involves a 3  $\mu$ M CHIR pulse between days 2 and 3. For DKK1 node with CHIR pulse, DKK1 (continuous) is induced on day 1 by adding 1  $\mu$ M GRZ, with 3  $\mu$ M CHIR pulse between days 2 and 3.
- (E) Representative images of Brachyury reporter (orange) on day 5, 2 days after the 3  $\mu$ M CHIR pulse. White arrows indicate Brachyury+ poles. Seeding: 100 (top) or 300 SBR mESCs (bottom). Scale bar: 200  $\mu$ m.
- (F) Representative images of Brachyury reporter (orange) on day 3, 2 days after induction of WNT3A from the organizer node. Starting conditions: 30 organizer cells with 100 (top) or 300 (bottom) SBR mESCs. Scale bar: 200  $\mu$ m.
- (G) Confocal sections of WNT3A node embryoid on day 4 (initial seeding: 300 WT mESCs, 30 WNT3A node, with 200 ng/mL DOX after day 1). Staining shows distribution of BRACHYURY (orange), CDX2 (red), and FOXA2 (cyan) (nuclei: gray). Scale bar: 50  $\mu$ m. Each image is representative of ~10 replicates. Right illustration shows primitive streak-like structure formation in WNT3A node-induced embryoid, including distinct anterior and posterior regions.
- See Figure S2 for detailed characterization of WNT3A node properties. Figure S3 includes replicates of (C)–(E).

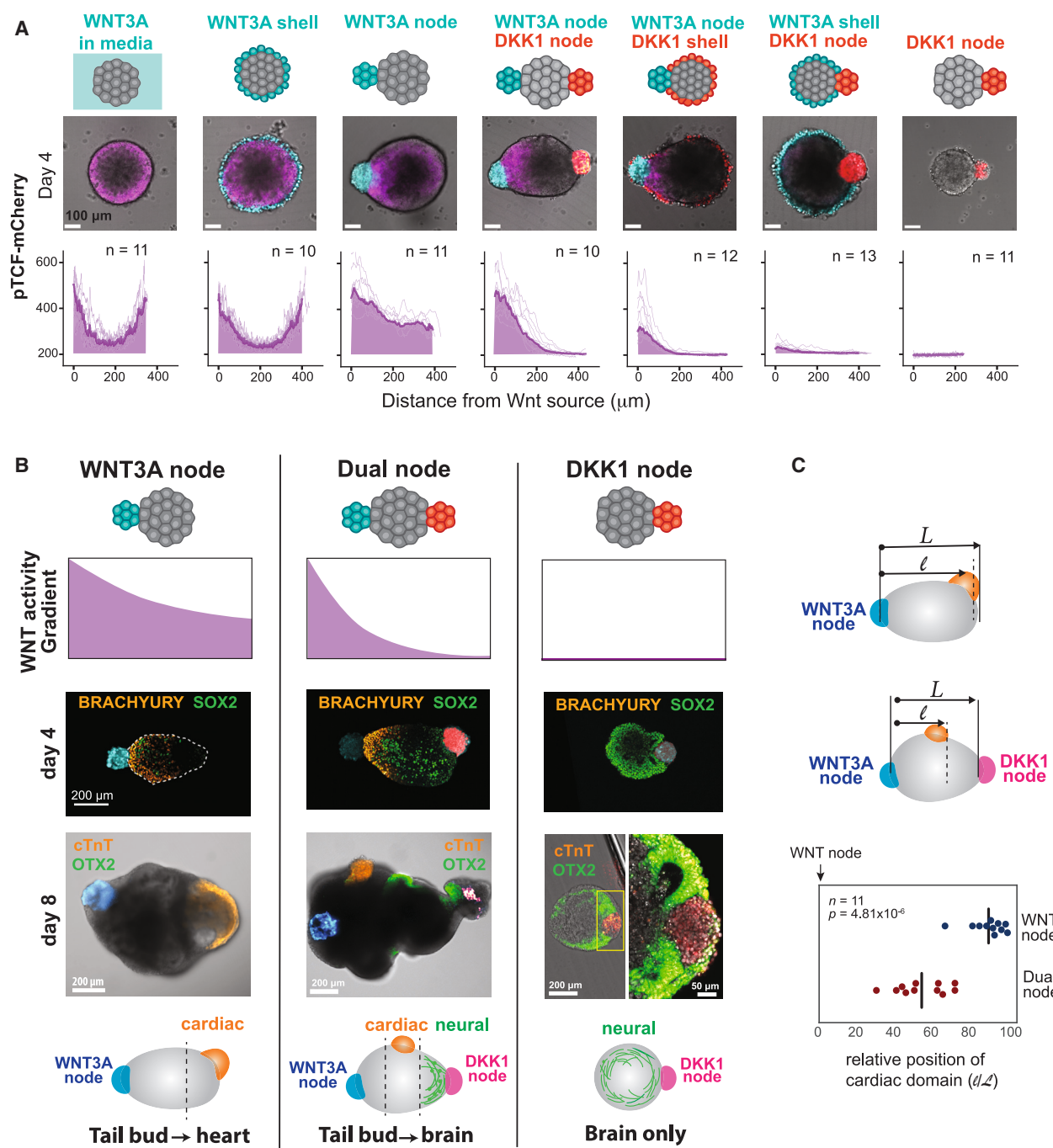


**Figure 3. Combinations of opposing synthetic organizers (WNT3A vs. DKK1) reshape morphogen gradients, yielding different ranges of anterior-posterior cell lineages**

(A) Comparison of pTCF-mCherry WNT activity reporter in mESC embryoids induced by different WNT3A sources, including WNT3A in media, WNT3A shell, WNT3A node, and their combinations. In each condition, WNT3A and/or DKK1 are induced starting on day 1 by adding 200 ng/mL DOX for WNT3A or 1  $\mu\text{M}$  GRZ for DKK1, respectively. Representative images and intensity profiles of pTCF-mCherry fluorescence on day 4 are shown. The bold line represents the mean of individual profiles ( $n = 10$ –13 per condition). Scale bar: 100  $\mu\text{m}$ . Note that DKK1 node-induced embryo shows considerably less growth, resulting in smaller length.

(B) Anterior-posterior axis formation in embryoids induced by WNT3A node, WNT3A/DKK1 dual nodes, and DKK1 node (initial seeding: 300 mESCs, 30 node cells for each node.). Top: a schematic of WNT activity gradient for each condition is shown in purple (based on A). Middle: confocal sections of BRACHYURY and SOX2 staining distributions for each condition on day 4. Bottom: cTnT (cardiac marker) and OTX2 (neural marker) staining distribution for day 8 embryos (see

(legend continued on next page)

the WNT3A node consistently induced a single Brachyury+ pole adjacent to the node, regardless of the initial ESC number (**Figures 2F** and **S3C**). The finding that the gastruloid protocol is less robust to starting conditions is consistent with recent studies that postulate that the CHIR pulse is required to generate a heterogeneous mix of Brachyury+ and Brachyury– ESCs, which subsequently differentially sort to opposing poles.<sup>28</sup> Thus, providing WNT3A from a spatially predetermined direction leads to spatially biased formation of a Brachyury+ pole, yielding more robust symmetry breaking.

These findings suggest that there could be a family of alternative ways to induce directionally biased polarization of the embryoid. For example, we tested what would happen if we combined a CHIR pulse with a DKK1 node (**Figures 2D** and **S3D**). This hybrid protocol generates embryoids with highly robust formation of a Brachyury+ pole, which always occurred on the opposite side from the DKK1 node, demonstrating that there are multiple and combinatorial strategies to generate a spatially biased morphogenetic gradient and response.

We next examined the structure of the Brachyury+ region of organizer-induced embryoids at a higher resolution (**Figure 2G**). In mouse embryos, specification of mesodermal and endodermal lineages occurs in a posterior-to-anterior arrangement within the primitive streak.<sup>29</sup> We observed that in the Brachyury+ region, cells proximal to the WNT3A node expressed Caudal type homeobox 2 (CDX2), reminiscent of the posterior primitive streak and tail bud.<sup>30,31</sup> More distal cells instead expressed Forkhead box protein A 2 (FOXA2), reminiscent of the anterior primitive streak and axial mesoderm.<sup>29,32</sup> Such patterning is analogous to the posterior region of developing embryo, with segregated expression of posterior (Cdx2) and anterior (FoxA2) primitive streak markers.

### Systematically reshaping the morphogen gradient using combinatorial synthetic organizers that produce the opposing factors WNT3A and DKK1

A unique advantage of synthetic organizer cells is that we can systematically tune the gradient shape by producing morphogens from diverse organizer architectures, as well as by providing multiple morphogens, such as WNT3A and its antagonist, DKK1. Thus, we created multiple dual organizers (**Figure 3A**): WNT3A node + DKK1 node, WNT3A node + DKK1 shell, and WNT3A shell + DKK1 node as well as a single DKK1 node. We used these different organizer configurations to drive the development of mESCs. For the dual-node structures, we focused here on those cases where the nodes were on roughly opposite sides of the structure, with an angular separation of 130°–180°. On day 4 after induction, we imaged the resulting WNT activity.

We found that the addition of the DKK1-producing organizers dramatically reshaped the WNT activity gradient (**Figure 3A**, pTCF reporter). The dual-node organizer structure yielded a WNT activity gradient with a far broader dynamic range

compared with a single WNT3A node case—there is equally high WNT activity proximal to the WNT3A node but much lower (essentially zero) WNT activity at the distal end, presumably blocked by the adjacent DKK1 node. By contrast, by day 4 and beyond, the single WNT3A node structure generated a shallower gradient with detectable intermediate levels of WNT activity at the distal end, leading to a smaller dynamic range. Both the WNT3A node + DKK1 shell and WNT3A shell + DKK1 node conformations also led to more restricted WNT activity gradients, albeit with a lower peak activity near the WNT3A organizer. Thus, the interplay of two opposing synthetic organizers yielded tunable gradient profiles across the embryoid. The single DKK1 node organizer did not induce pTCF activity or any increase in embryoid size or elongation (**Figures 3A** and **3B**).

Together, these data show that different synthetic organizer architectures can be employed to systematically sculpt the WNT activity gradient in an embryoid. The resulting set of WNT activity gradients exhibits diverse quantitative features: the gradient can span either a small or large range (the range of highest to lowest WNT activity experienced within the embryoid) and can have different steepness (the change in WNT activity over a given length within embryoid).

### The morphogen gradient range determines the resulting spectrum of A-P cell lineages

We then followed the development of these organizer-induced embryoids using an mESC line containing early cell fate reporters: Brachyury, a marker for primitive streak (precursor to mesoderm and endoderm), and Sox1, a marker for neuronal ectoderm.<sup>26,27</sup> Here, we focused on embryoids generated by a single WNT3A node, a single DKK1 node, and WNT3A/DKK1 dual-node organizers. The single WNT3A node induces Brachyury+ cells (orange) without any detectable Sox1 induction. By contrast, the single DKK1-producing node only generates Sox1+ cells (green) without Brachyury+ cells. However, in embryoids induced by opposing WNT3A and DKK1 nodes, we observed the simultaneous induction of Brachyury+ cells and Sox1+ cells within the same structure (**Figure S4A**, with Brachyury signal closer to the WNT3A node and Sox1 signal closer to the DKK1 node).

In dual-node structures, the timing of morphogen production by each of the two nodes could be precisely controlled by independent chemical inducers (DOX for WNT and GRZ for DKK1). We therefore tested the effect of delayed DKK1 induction by 0, 1, 2, and 3 days after WNT3A induction (**Figure S4B**). We found that variations in timing could alter the balance between resulting Brachyury+ and Sox1+ cells. With no delay (0 days), Sox1+ cells were dominant by day 8. By contrast, with a delay of DKK1 induction of 3 days, Brachyury+ cells were dominant. However, a 1- or 2-day delay resulted in a more balanced outcome, with significant numbers of both Brachyury+ cells and Sox1+ cells in the same embryoid (**Figure S4B**). For subsequent dual-node

**Video S2** for live imaging of beating). Inset for DKK1 node-induced embryoid shows zoomed view of OTX2-positive cells adjacent to DKK1 node. Scale bar: 200 μm (inset: 50 μm).

(C) Quantification of relative position of beating cardiac domain along the long axis of WNT3A node or dual-node-induced embryoids. *p* value:  $4.81 \times 10^{-6}$  (*n* = 11), unpaired *t* test.

See **Figure S4** for optimizing conditions using reporter lines.

experiments, we used a 1-day delay between WNT3A (day 1) and DKK1 (day 2) induction to favor this balance in cell lineages.

With all three organizer conformations, cell fates along the WNT activity gradient in the embryoids seem to mirror the native A-P patterning observed in mouse embryos. We further characterized the A-P axis in our embryoids: BRACHYURY marks the posterior primitive streak,<sup>33</sup> while SPY-box 2 (SOX2) marks an anterior ectoderm (Figure 3B).<sup>34</sup> WNT3A node embryoids showed BRACHYURY+ cells close to the WNT3A node and few SOX2-positive cells (around the center of embryoid, often adjacent to the BRACHYURY-positive cells). By contrast, a DKK1 node shifted most mESCs to a SOX2+ ectodermal fate. The dual-node embryoid showed balanced distributions of BRACHYURY and SOX2, with BRACHYURY closer to the WNT3A node and SOX2 expressed both around the center and next to the DKK1 node.

We then examined more differentiated cell types, such as cardiac and neural cells, in later-stage embryoids (day 8) by staining for the cardiac marker, cardiac troponin (cTnT),<sup>35</sup> and the anterior neural marker, Orthodenticle homeobox 2 (OTX2).<sup>36,37</sup> In WNT3A node embryoids, the cTnT+ cardiac tissue arose opposite the WNT3A node, at the anterior end (Figures 3B and 3C). OTX2+ cells were absent, consistent with a truncated A-P axis. DKK1 node embryoids lacked cTnT+ cells, highlighting the need for WNT signaling to induce cardiac cell. Notably, however, these embryoids had many OTX2+ cells, and those closest to the DKK1 node formed a rosette-like arrangement, resembling a neuroepithelium (Figure 3B).<sup>38</sup> Dual-node embryoids showed a broader range of A-P lineages, with OTX2+ cells observed adjacent to the DKK1 node and cTnT+ cardiac cells arising in a distinct localized cluster midway between the two nodes (Figures 3B and 3C). Thus, the dual-node structure appears to yield a broader range of cell fates along the A-P axis, combining aspects of both single-node structures and consistent with the higher dynamic range of WNT activity. The single-node embryoids, by contrast, show differentially truncated A-P fates: the WNT3A single-node embryoids lack head-like tissues, while the DKK1 single-node embryoids only show head-like tissues.

### scRNA-seq analysis of cell-type diversity in synthetic organizer-induced embryoids

To more comprehensively examine the cell-type diversity in the organizer-induced embryoids, we performed single-cell RNA sequencing (scRNA-seq) on the day 8 embryoids induced by a single WNT3A node, a single DKK1 node, and dual nodes (WNT3A + DKK1). UMAP analysis (Figure 4A) and analysis of key marker genes (Table S1) revealed distinct lineage outcomes for each configuration. Single WNT3A node embryoids showed a diverse array of well-differentiated mesodermal lineages (45.5%) but relatively rare endodermal cell types and few, less differentiated ectodermal cell types (15.6%) (Figures 4B and S5A). By contrast, single DKK1 node embryoids lacked mesoderm entirely and instead displayed a range of neuroectodermal fates (Figure 4B). Notably, the dual-node embryoids had both mesodermal (66.3%) and ectodermal (27.7%) lineages (Figures 4B and S5A). In short, the dual-node embryoids generated a cell-type spectrum encompassing features of both the WNT3A and DKK1 node embryoids, more closely recapitulating the full complement of cells found in natural embryos.

Similarity analysis comparing our synthetic organizer-induced embryoids (at day 8) to natural E6.5–E8.5 mouse embryo data<sup>39</sup> corroborated our lineage annotations and reinforced the notion that dual-node embryoids span a wider range of mesodermal and ectodermal lineages (Figure 5A). In the single WNT3A node embryoids, only mesodermal lineages showed a high similarity to mouse embryos. By contrast, with the dual-node embryoids, both ectodermal and mesodermal lineages showed high similarity to the mouse embryo.

Importantly, these results also highlight the cell types of the E6.5–E8.5 stage embryo that we are unable to recapitulate by solely modulating the WNT signaling gradient. For example, endodermal cells were underrepresented in our models. We confirmed limited expression of the endodermal marker SOX17 in the WNT3A node embryoids on day 6 (Figure S5C), suggesting that WNT3A favors mesoderm over endoderm differentiation in our system. We hypothesize that additional signals, such as Activin, may be required to promote endoderm differentiation.<sup>40</sup> We therefore developed an Activin A-producing node to test this. Following Activin A induction, we observed an increased proportion of SOX17+ FOXA2+ double-positive endoderm cells, which localized at the surface of the embryoid (Figure S5C).<sup>41</sup> This preliminary result indicates that the Activin A node can favor endodermal differentiation in a spatially restricted manner. These findings demonstrate that this synthetic organizer system can be used to pattern different morphogens, which can enable distinct cellular differentiation routes within the embryoid.

### Identification of highly localized cell-type lineages

Several mesodermal cell types in our synthetic organizer-induced embryoids strongly match the identity of cells in mouse embryos, including cardiac cells, endothelial cells, primitive blood (e.g., primitive erythrocytes and hemogenic endothelium), and primordial germ cells (PGCs). These high-matching lineages are found in both the WNT3A node and dual-node embryoids (Figure 5A). Given how well these lineages matched true embryonic cells, we were curious to identify their localization within the WNT3A node embryoids (Figures 5B–5D).

The scRNA-seq data demonstrated the presence of embryonic blood cells marked by the expression of the blood progenitor markers runt-related transcription factor 1 (*Runx1*) and GATA-binding protein 1 (*Gata1*), along with the embryonic hemoglobin isoforms hemoglobin Y, beta-like embryonic chain (*Hbb-y*), hemoglobin Z, beta-like embryonic chain (*Hbb-bh1*), and hemoglobin alpha, adult chain 2 (*Hba-a2*). To assess the localization of these embryonic blood cells, we stained for RUNX1 and GATA1 and found that cells co-expressing these two factors form a cluster, structurally resembling a blood island (regions in early embryos that contain hematopoietic and endothelial precursor cells that localize posterior to the beating cardiac region [Figure 5B]).<sup>42</sup>

We also identified a distinct cluster of PGC-like cells—precursors to the gametes—in our scRNA-seq data, marked by expression of *Nanog* and *Prdm1*.<sup>43,44</sup> Immunostaining of NANOG and B lymphocyte-induced maturation protein 1 (BLIMP1), both PGC markers, showed that these PGC-like cells form a tight cluster close to but not directly adjacent to the WNT3A node (Figure 5C).

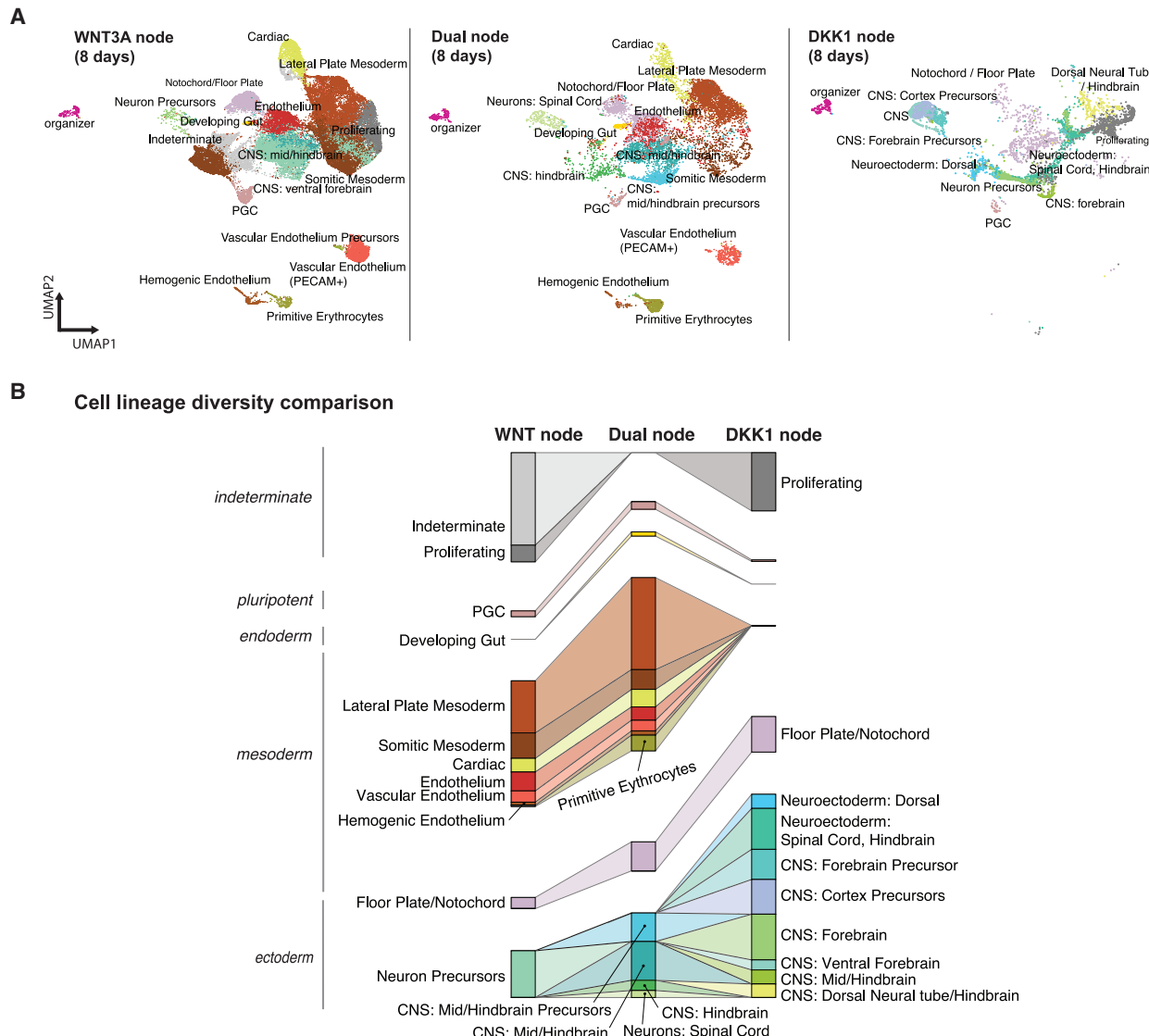


**Figure 4. Cell-type diversity in synthetic organizer-induced embryoids**

(A) UMAP graph representing cell clusters identified in scRNA-seq of WNT3A node embryoid (35,974 sequenced cells), WNT3A/DKK1 dual nodes embryoid (9,902 sequenced cells), and DKK1 node embryoid (4,464 sequenced cells) on day 8. See Table S1 for key marker genes used to annotate cell identity in each cluster.

(B) An alluvium plot comparing cell lineage diversity across conditions. The Wnt and dual-node embryoid datasets were down-sampled to match the number of cells in the DKK1 node embryoid dataset. WNT3A node embryoid contains mostly mesodermal lineages, whereas DKK1 node embryoid mostly has ectodermal cells. Only dual nodes embryoid has matured lineages from both mesodermal and ectodermal cells.

See also Figures S5A and S5B for the distribution of three germline lineages.

Finally, the scRNA-seq shows native-like cardiac cells, associated with the pan-cardiac markers *Nkx2-5* (homeobox transcription factor regulating heart development) and cardiomyocyte marker *Tnnt2* (cardiac muscle troponin T, aka cTnT), as well as the ventricular markers myosin light chain 2 (*Myl2*) and iroquois homeobox 4 (*Irx4*).<sup>35</sup> Staining for NKX2.5 and cTnT showed their association with a large cardiac-like structure at the opposite end of the embryoid from the WNT3A node (Figure 5D).

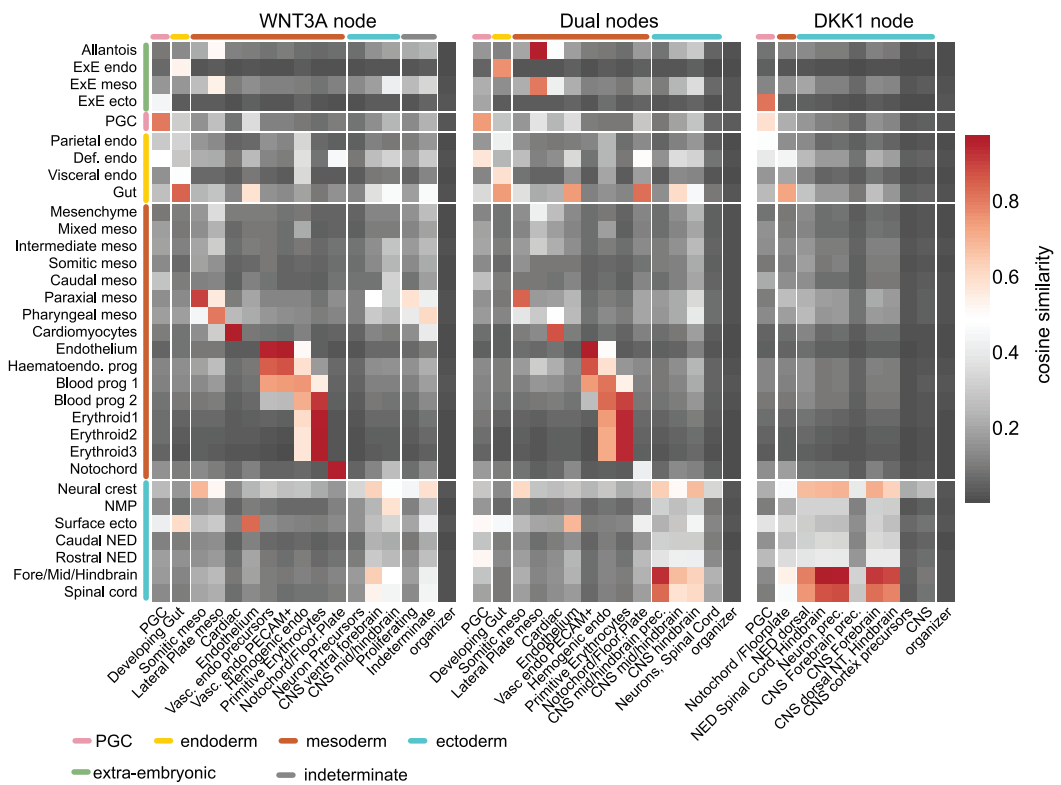
In summary, we find that the synthetic organizer-induced embryoids contain multiple mesoderm-derived cell types that

closely match native embryonic cells and that these form tightly localized structures within the embryoid.

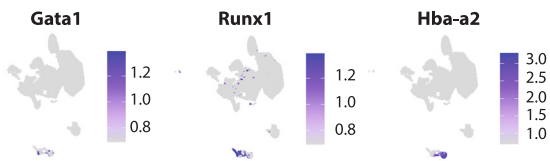
#### A shallower Wnt activity gradient yields more complex cardiac and endothelial structures

We were intrigued by the presence of these native-like cardiac cells in the WNT3A node embryoids and the fact that these formed a large, ordered structure compared with the cardiac region observed in the dual-node embryoids. We hypothesized that the shallower gradient generated by the single WNT3A

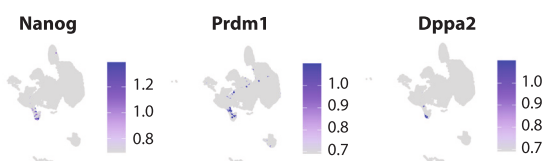
### A Cell type comparison: mouse embryo vs synthetic organizer induced embryoids



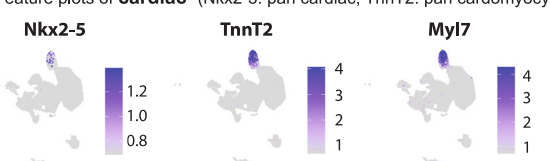
**B** Feature plots of **hematopoietic** (blood progenitor: Gata1, Runx1, embryonic hemoglobin isoform: Hba-a2)



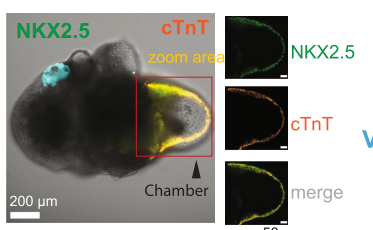
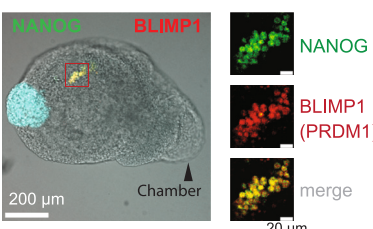
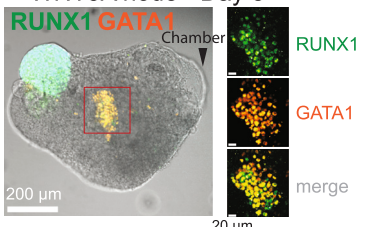
**C** Feature plots of **Primordial Germ Cells PGCs** (Pluripotent: Nanog, Primordial germ layer: Prdm1, Dppa2)



**D** Feature plots of **cardiac** (Nkx2-5: pan cardiac, TnnT2: pan cardiomycyte)



**WNT3A node - Day 8**



Video S3

(legend on next page)

node while truncating more anterior cell fates might lead to higher resolution of differentiation and morphogenetic cooperation within narrower regions of the A-P axis (Figure 6A).

To better track cardiac and endothelial development in the WNT3A node embryos, we used a mesodermal reporter mESC line (Kdr reporter). Kdr+ cells differentiate into either cardiac or endothelial cells.<sup>45</sup> Time-lapse imaging with the Kdr reporter line showed a strong Kdr induction by day 4, followed by the reorganization of Kdr+ cells toward the distal end (away from the WNT node) and organization into what appears to be a chambered structure (Figures 6B and 6C). By contrast, embryos treated with soluble WNT3A failed to self-organize, and Kdr expression diminished by day 8. Live-cell imaging revealed that this Kdr+ structure showed consistent beating (Video S4) and was associated with a broader network of Kdr+ cells, which we postulated to be a vascular network.

Looking at a larger number ( $n = 93$ ) of WNT3A embryos, 73% developed a localized beating structure, and 12% formed a beating cavity or chamber (Figures 6D and S6A). We confirmed this phenotype with two distinct, independently derived mESC lines (E14Tg2A and CGR8), which showed similar cardiac development frequencies (75% of E14Tg2A line and 73% of CGR8 line, Figure S6B). 3D reconstruction of actin networks (phalloidin) and nuclei (DRAQ5) revealed that these beating chambers are fully enclosed by cells (Figure 6E; Video S5), with a central cell-free space. Calcium imaging using Fluo-4 AM dye showed calcium-associated beating with a highly consistent period of ~1.4 s (42 beats per minute) (Figures 6F, 6G, and S6A).

We further stained these structures for the cardiac markers cTnT and the endothelial marker platelet and endothelial cell adhesion molecule 1 (PECAM1) to study the relative localization of the two populations.<sup>46</sup> The main chamber clearly stained for cTnT, confirming its cardiac identity, while PECAM1 stained a network of cells that emanated from the cTnT+ chamber (Figure 6H). This staining is consistent with the formation of an extensive endothelial network associated with the cardiac-like chamber but which emanates further out into the embryo.

Thus, the WNT3A node gives rise to a remarkably ordered, multi-cell-type structure that integrates a beating, chambered cardiac assembly with a vascular endothelial network. Even more remarkable is that this complex structure arises through self-organization, distinct, for example, from “assembloids,” which are created by mixing pre-differentiated cell lineages.<sup>47,48</sup> It is also notable that although the dual-node embryos formed a localized beating cardiac structure (Figures 3B and S4C), this is much smaller and never shows formation of a chamber or inte-

gration with a clear endothelial network. These observations are consistent with a model in which the shallow WNT gradient plays a central role in generating the proper mix and arrangement of cell types required for this more complex, high-resolution developmental process.

Many studies suggest that cardiac development involves factors beyond WNT, including bone morphogenetic protein (BMP), vascular endothelial growth factor (VEGF), and fibroblast growth factor (FGF).<sup>49,50</sup> Both *in vivo* and *in vitro* cardiogenesis require precise dosages of WNT and BMP signaling in opposing gradients.<sup>51</sup> We speculated that secondary morphogens may be induced within our WNT3A node embryos to stimulate cardiac development. Our scRNA-seq data suggest an upregulation of *Bmp4* specifically in the cardiogenic cells (Figure S6C). RNA *in situ* hybridization identified that *Bmp4* expression localized far from the WNT3A node on day 8, particularly in cTnT+ cardiomyocytes. Furthermore, to test if BMP signaling was necessary for cardiac structure formation, we treated these embryos with a BMP signaling inhibitor, LDN193189, in the media. Inhibiting BMP signaling before day 6 completely blocked the formation of the beating domain in WNT3A node embryos (Figure S6D).

Continued WNT3A production from the node organizer could also play a role in forming a beating cardiac domain. To assess this, we investigated how the duration of WNT3A production from the synthetic organizer affects the formation of a beating domain. Removing the WNT3A node before day 4 by activating the suicide switch significantly decreased the frequency of beating domain formation (removed day 2: 12%, removed day 3: 23%, Figure S6E), indicating that 3–4 days of exogenous WNT3A production are critical for consistent cardiac development.

In summary, the shallow WNT gradient generated by the single WNT3A node consistently drives the formation of a locally ordered, chambered, heart-like structure exhibiting regular Ca<sup>2+</sup>-associated beating, integrated with a vascular network. While driven by the WNT gradient, this process involves the secondary induction of localized signaling centers, including *Bmp4* production. We propose that the shallow WNT gradient provides higher-resolution morphogenetic information, facilitating the precise spatial arrangement of cell types necessary for forming this complex structure.

## DISCUSSION

### Programming synthetic organizer cells that adopt diverse spatial architectures around progenitor cells

Here, we report a cell engineering approach to reconstruct spatially defined developmental environments around ESCs

**Figure 5. Cell-type comparison between mouse embryo and synthetic organizer-induced embryoids and spatial characterization of key lineages**

- (A) Similarity heatmap between expression profiles of cell lineages in synthetic organizer-induced embryoids and mouse embryo (E6.5–E8.0). Plot is organized by germline lineages (color-coded on left axis); endo, endoderm; meso, mesoderm; ecto, ectoderm; NED, neuroectoderm; NT, neural tube; NMPs, neuro-mesodermal progenitors; prec., precursors; and prog., progenitors.
- (B) Feature plots (left) and immunostaining (right) of hematopoietic markers. RUNX1/2/3 (green) and GATA1 (red) expressing cells show a localized cluster within WNT3A node-induced embryoid on day 8, analogous to early blood island. Node is shown in cyan. Scale bar: 200 μm (inset: 20 μm).
- (C) Feature plots (left) and immunostaining (right) of primordial germ cell (PGC) markers. Nanog (green) and BLIMP1 (red) expressing cells form a localized cluster within WNT3A node-induced embryoid on day 8. Scale bar: 200 μm (inset: 20 μm).
- (D) Feature plots (left) and immunostaining (right) of myocardial markers. NKX2.5 (green) and cTnT (red) within WNT3A node-induced embryoid shows localized expression only around the heart-like chamber. Scale bar: 200 μm (inset: 50 μm). See [Video S3](#) for 3D reconstructed image.

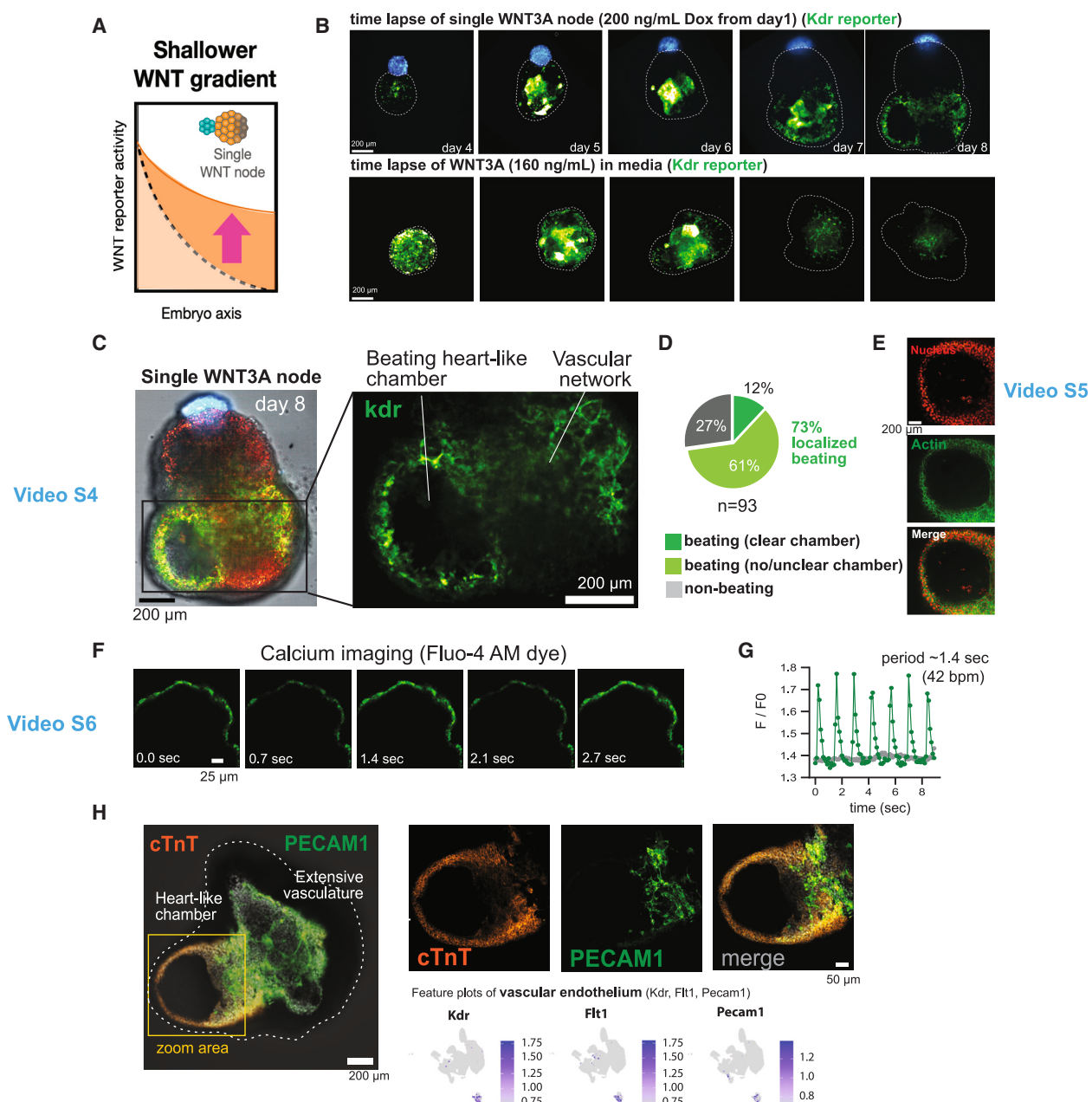


**Figure 6. Shallow gradient from single WNT3A node yields development of beating and chambered cardiac structure**

- (A) WNT3A node generates a much shallower gradient (dark) compared with WNT3A/DKK1 dual node (light), potentially providing higher-resolution positional information.
- (B) Time-lapse imaging of Kdr-EGFP reporter line treated with WNT3A node (top) or WNT3A in media (bottom), from days 4 to 8. Both conditions are seeded with 300 mESCs. The WNT3A node is seeded with 30 cells and induced with 200 ng/mL DOX on day 1. For the WNT3A in media condition, 160 ng/mL of mouse WNT3A is added to the media on day 1. Scale bar: 200  $\mu$ m.
- (C) Kdr-EGFP distribution on day 8 in WNT3A node-induced embryooid. Kdr-positive cells are localized on the opposite side of the WNT3A node and form vascular-like network and a beating chamber. See *Video S4* for live imaging.
- (D) Pie chart depicting distribution of beating phenotypes. About 73% of WNT3A node-induced embryooids showed localized beating regions, and 12% showed clear beating chamber structure.
- (E) Distribution of actin (stained with phalloidin-Alexa 488) and nucleus (stained with DRAQ5) showed heart-like chamber is fully enclosed and has no internal cellular structures. See *Video S5* for 3D reconstructed image. Scale bar: 200  $\mu$ m.
- (F) Calcium imaging of a beating domain on day 8 using a Fluo-4 AM calcium dye. See *Video S6* for live imaging.
- (G) An intensity profile of Fluo-4 AM dye shows regular oscillation of calcium concentration in the beating domain.

(legend continued on next page)

*in vitro* using synthetic organizer cells. This approach integrates Spemann and Mangold's organizer concept<sup>3</sup> with Steinberg's differential adhesion principles,<sup>52</sup> harnessed with modern syn-CAMs.<sup>13</sup> By using a library of natural and synthetic CAMs, we can engineer cell lines to self-organize around ESCs in distinct and precise ways, creating diverse organizer architectures, such as anisotropic nodes, isotropic shells, or multi-node/mixed node-shell architectures. Spatial localization of these organizers is a relatively autonomous process requiring minimal user intervention, making this approach amenable to high-throughput studies.

### Synthetic organizers yield tunable spatiotemporal control over morphogen signaling

Living cells can be used as a source of morphogens.<sup>53,54</sup> Here, by using a cell line whose adhesion properties we can manipulate, we can dictate the position of morphogen-producing cells around the progenitor cells, creating custom morphogen gradients. By coordinating organizers to secrete antagonistic or complementary morphogens like WNT3A and DKK1, we can further increase the combinatorial complexity of these gradients.

We also incorporate drug-inducible systems to precisely control the timing and amplitude of morphogen induction, as well as terminate organizer signaling through activating a cellular suicide switch. This composite spatial and temporal control that a living cell can exert, represents a distinct capability compared with soluble morphogens or morphogen delivery from non-living materials like beads.

### Systematically driving development along different paths

Our synthetic organizer system sculpts diverse morphogen landscapes in a controlled manner. This enables systematic interrogation of how cells interpret and respond to positional cues during patterning and morphogenesis. In this study, we focused on varying the shapes of WNT activity gradients and their developmental consequences.

Combining the WNT3A and DKK1 nodes generated a WNT activity gradient spanning from high activity at one pole to undetectable levels at the opposite pole. This gradient induced a diverse spectrum of cell lineages within the same embryoid, including mesoderm lineages proximal to the high WNT activity and ectoderm lineages near the low WNT signal, reflecting A-P anatomical organization. By contrast, a single WNT3A node produced a shallower WNT gradient, truncating ectodermal lineages but inducing a localized beating, chambered, heart-like beating structure within the embryoid. This suggests that the shallow gradient encodes higher-resolution positional information, yielding the required range and fine spatial organization of cell types necessary for more native-like cardiac development. Supporting this, the WNT3A node alone triggered a cascade of downstream events within the embryoid, including production of Bmp4, a key morphogen in cardiogenesis.<sup>51</sup>

(H) Feature plots (left) and immunostaining (right) of cardiac and vascular endothelial markers. Cardiomyocytes (cTnT-positive cells, orange) are localized around the chamber. The vascular network (PECAM1-positive cells, green) extends out from the base of the cardiac chamber into the rest of the embryoid. Scale bar: 200  $\mu$ m (inset: 20  $\mu$ m).

See also Figure S6 for reproducibility and further analysis on cardiac beating phenotypes.

A key advantage of synthetic organizers is the ability to tune the range of resulting lineages by finely titrating the morphogen landscape in 3D (Figure 7). This offers an alternative to current *in vitro* models, such as lineage-specific differentiation protocols or protocols for gastruloids or synthetic embryos,<sup>55,56</sup> which lack the programmability of the synthetic organizers. Notably, the orthogonality of our L929-based synthetic organizers is unique compared with other cell-based signaling centers, such as ESCs engineered to express Sonic hedgehog (SHH) or WNT/NODAL.<sup>53,54</sup> These stem cell-based signaling centers lack programmed control over spatial organization and also eventually differentiate into other lineages, which could interact with target progenitor cells in unintended ways. The synthetic organizers used here, by contrast, enable systematic exploration of the "morpho-space" by providing diverse developmental instructions guided by user-defined positional cues. In addition, this approach is potentially compatible with other methods—it may be beneficial to combine engineered organizer cells with soluble factors (as observed by combining the DKK1 node with CHIR stimulation, Figure 2D) or extra-embryonic cells.

### Future potential uses of synthetic organizer cells

Unlike user-directed 3D bioprinting approaches,<sup>57</sup> self-assembling synthetic organizers could improve consistency for developmental models, disease studies, or therapeutic screening. Synthetic organizer cells may prove more accessible than other protocols relying on expensive purified morphogens or complicated equipment.

A hallmark of synthetic organizers is their tunability and programmability. By using different organizer architectures and morphogen combinations, one can systematically change the developmental context, generating diverse morphogenetic outcomes across many progenitor cell types. This offers new ways to study fundamental developmental processes: instead of tracking one natural trajectory, we can systematically generate sets of alternative trajectories and better understand how developmental landscapes guide and keep morphogenesis on track in a reproducible manner.<sup>2,58,59</sup>

This system might eventually aid in the generation of tissues or organs with tailored morphologies for clinical applications, such as transplantation. Ultimately, elements of these approaches could contribute to regenerative development *in vivo*. If organizer cells could recognize sites of injury, they might be able to reconstitute regenerative morphogenetic cues *in situ*.

### Limitations of the study

From a developmental characterization standpoint, we lack detailed spatial mapping of the cell types identified through scRNA-seq within the embryoids, as well as insights on how this cellular patterning emerges over time. Employing techniques like spatial transcriptomics or proteomics<sup>60–63</sup> or sequencing over different time points or lineages<sup>64–68</sup> could provide more comprehensive insights. Additionally, our U-bottom 96-well

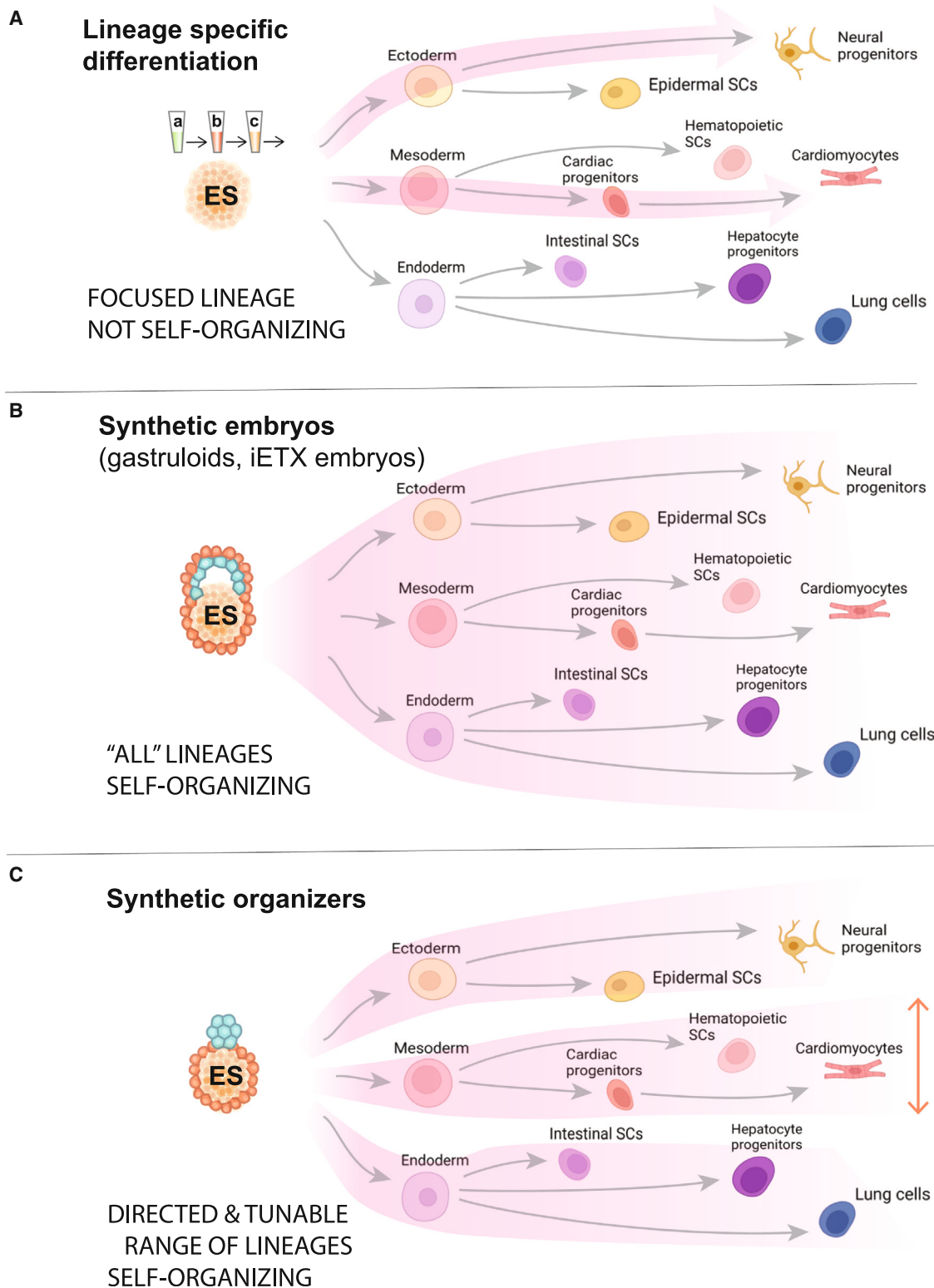


**Figure 7. Synthetic organizers provide platform to flexibly direct and tune *in vitro* development**

(A) Lineage-specific differentiation: ESCs are differentiated into specific lineages using defined differentiation protocol. This method generates a uniform population of a specific cell lineage and does not involve self-organization.

(legend continued on next page)

format limits embryoid size at later time points. Exploring improved culture conditions, e.g., shaking or roller bottles,<sup>69</sup> could promote further development.

From an engineering perspective, there are countless forward-looking opportunities to enhance synthetic organizers. As cell engineering tools continue advancing,<sup>70–72</sup> it will become possible to engineer more refined and complex organizer architectures. Our current approach also requires expressing the synCAM ligand on the progenitor cells, but targeting native ligands could circumvent this requirement. In addition to WNT3A, DKK1, and activin A, there are many other morphogens that would be interesting to utilize in the organizer. We have also not fully explored optimization of the organizer cell platform—it is possible that other cell lines may have advantages, and it may be helpful to knock out undesired endogenous signals in L929 cells and to modulate the growth of the organizer cells. Finally, our approach could be improved further by creating more dynamic synthetic organizers functioning in a stepwise manner, by replacing a first organizer with a second one using the suicide switch, or by creating organizers that recognize later-stage-specific ligands. Such approaches could yield synthetic developmental cascades. This study serves as a proof of concept for the synthetic organizer approach. Continued advances in synthetic biology tools offer potential solutions to address many of these challenges.

## RESOURCE AVAILABILITY

### Lead contact

Further information and requests for resources and reagents should be directed to and will be fulfilled by the lead contact, Wendell Lim ([wendell.lim@ucsf.edu](mailto:wendell.lim@ucsf.edu)).

### Materials availability

All cell lines and plasmids generated in this study are available from the [lead contact](#) with a completed Materials Transfer Agreement. Plasmids generated in this study will be deposited to Addgene. Addgene IDs are available in the [key resources table](#).

### Data and code availability

All original codes will be deposited on Zenodo (Zenodo: 12642864. <https://zenodo.org/doi/10.5281/zenodo.12642864>).

scRNA-seq and bulk RNA-seq data collected for this paper will be deposited at GEO (GEO: GSE244033).

Any additional information required to reanalyze the data reported in this paper is available from the [lead contact](#) upon request.

## ACKNOWLEDGMENTS

This work was supported by the following grants: RO1 DK130969 (W.A.L. and O.D.K.), RO1 HL114948 (B.G.B.), and R35 DE026602 (O.D.K.) awarded by The National Institutes of Health and DBI-1548297 (W.A.L.) awarded by the National Science Foundation. We thank the UCSF Cell Design Institute and ValhallaFoundation for their support. We thank D. Vaka, S. Toda, P. Lopez, S. Sidhu, P. Marangoni, F. Fattahai, R. Almeida, N. Blizzard, and members of the Klein and Lim labs for assistance and advice and Z. Weinberg and S. Soliman for providing plasmids for the GRZ-inducible system. The Nikon Imaging

Center at UCSF assisted with immunostaining data acquisition. We thank the UCSF Genomic Colab for scRNA-seq sample preparation and the UCSF CAT for sequencing services.

## AUTHOR CONTRIBUTIONS

Conceptualization, W.A.L. and O.D.K.; methodology, T.Y., C.T., J.M.B., A.J.S., Y.X., D.B., I.M., P.K., N.P.S., and A.A.; investigation, T.Y., C.T., J.M.B., B.G.B., and D.B.; writing, T.Y., C.T., J.M.B., A.J.S., B.G.B., D.B., O.D.K., and W.A.L.; funding acquisition, W.A.L., O.D.K., and B.G.B.; resources, W.A.L., O.D.K., and D.B.; supervision, W.A.L., O.D.K., and D.B.

## DECLARATION OF INTERESTS

B.G.B. is a founder and shareholder of Tenaya Therapeutics. W.A.L. is a shareholder of Gilead Sciences, Intellia Therapeutics, Allogene Therapeutics, and SciFi Foods. W.A.L. has been an advisor to Cell Design Labs, Kite Therapeutics, Allogene Therapeutics, and SciFi Foods; is on the Board of the Burroughs Wellcome Fund; and is on the Editorial Board of *Cell*. T.Y., C.T., J.M.B., A.J.S., O.D.K., and W.A.L. have applied for patents related to this work.

## DECLARATION OF GENERATIVE AI AND AI-ASSISTED TECHNOLOGIES IN THE WRITING PROCESS

During the preparation of this work, some authors used perplexity.ai to improve readability. After using this tool, the authors reviewed and edited the content as needed and take full responsibility for the content of the published article.

## STAR METHODS

Detailed methods are provided in the online version of this paper and include the following:

- [KEY RESOURCES TABLE](#)
- [EXPERIMENTAL MODEL AND SUBJECT DETAILS](#)
  - Cell lines and culture conditions
- [METHOD DETAILS](#)
  - Gene construction and cloning
  - Establishing synthetic organizer cell lines – lentivirus transduction
  - Establishing mESC lines - transduction plasmids using Nucleofection
  - Synthetic organizer architecture construction around a mESC core and morphogen induction
  - Generating Gastruloid
  - Live imaging
  - Calcium imaging
  - Immunostaining
  - Whole mount RNAscope staining
  - Imaging fixed samples
  - MULTI-seq sample preparation
  - scRNA-seq processing, clustering, and plotting of data
  - Comparison of cell types from organized embryos with cell types from natural mouse embryos and gastruloids
  - Bulk RNA-seq sample preparation and sequencing
- [QUANTIFICATION AND STATISTICAL ANALYSIS](#)
  - Statistical analysis
  - Quantification of organizer geometries
  - Analyzing Positions and Morphologies
  - Measuring relative positions of two nodes on embryoid
  - Quantification of major and minor axis of embryos

(B) Synthetic embryos (e.g., iETX embryos and gastruloids): these approaches are aimed at generating a broad spectrum of lineages that self-organize in a manner that mimics natural embryogenesis.

(C) Synthetic organizers: this approach provides tunable and directed control over the range of lineages and further cell, including associated lineages that can self-organize into more complex multi-cell-type structures. Synthetic organizers may offer enhanced flexibility and control in *in vitro* developmental processes.

- Plotting reporter signals
- Measuring beating cardiac positions in embryoid

#### SUPPLEMENTAL INFORMATION

Supplemental information can be found online at <https://doi.org/10.1016/j.cell.2024.11.017>.

Received: September 26, 2023

Revised: July 10, 2024

Accepted: November 8, 2024

Published: December 19, 2025

#### REFERENCES

1. Shahbazi, M.N., Siggia, E.D., and Zernicka-Goetz, M. (2019). Self-organization of stem cells into embryos: A window on early mammalian development. *Science* **364**, 948–951. <https://doi.org/10.1126/science.aax0164>.
2. Trentesaux, C., Yamada, T., Klein, O.D., and Lim, W.A. (2023). Harnessing synthetic biology to engineer organoids and tissues. *Cell Stem Cell* **30**, 10–19. <https://doi.org/10.1016/j.stem.2022.12.013>.
3. Spemann, H., and Mangold, H. (1924). über Induktion von Embryonalanlagen durch Implantation artfremder Organisatoren. *Arch. Für Mikrosk. Anat. Entwicklungsmechanik* **100**, 599–638. <https://doi.org/10.1007/BF02108133>.
4. Fuchs, E., Tumbar, T., and Guasch, G. (2004). Socializing with the Neighbors: Stem Cells and Their Niche. *Cell* **116**, 769–778. [https://doi.org/10.1016/S0092-8674\(04\)00255-7](https://doi.org/10.1016/S0092-8674(04)00255-7).
5. Briscoe, J., and Small, S. (2015). Morphogen rules: design principles of gradient-mediated embryo patterning. *Development* **142**, 3996–4009. <https://doi.org/10.1242/dev.129452>.
6. Capek, D., Smutny, M., Tichy, A.-M., Morri, M., Janovjak, H., and Heisenberg, C.-P. (2019). Light-activated Frizzled7 reveals a permissive role of non-canonical wnt signaling in mesendoderm cell migration. *eLife* **8**, e42093. <https://doi.org/10.7554/eLife.42093>.
7. Gurdon, J.B., Mitchell, A., and Mahony, D. (1995). Direct and continuous assessment by cells of their position in a morphogen gradient. *Nature* **376**, 520–521. <https://doi.org/10.1038/376520a0>.
8. Manfrin, A., Tabata, Y., Paquet, E.R., Vuaridel, A.R., Rivest, F.R., Naef, F., and Lutolf, M.P. (2019). Engineered signaling centers for the spatially controlled patterning of human pluripotent stem cells. *Nat. Methods* **16**, 640–648. <https://doi.org/10.1038/s41592-019-0455-2>.
9. Nowak, M., Machate, A., Yu, S.R., Gupta, M., and Brand, M. (2011). Interpretation of the FGF8 morphogen gradient is regulated by endocytic trafficking. *Nat. Cell Biol.* **13**, 153–158. <https://doi.org/10.1038/ncb2155>.
10. Sako, K., Pradhan, S.J., Barone, V., Inglés-Prieto, Á., Müller, P., Ruprecht, V., Capek, D., Galande, S., Janovjak, H., and Heisenberg, C.-P. (2016). Optogenetic Control of Nodal Signaling Reveals a Temporal Pattern of Nodal Signaling Regulating Cell Fate Specification during Gastrulation. *Cell Rep.* **16**, 866–877. <https://doi.org/10.1016/j.celrep.2016.06.036>.
11. Amadei, G., Handford, C.E., Qiu, C., De Jonghe, J., Greenfeld, H., Tran, M., Martin, B.K., Chen, D.-Y., Aguilera-Castrejon, A., Hanna, J.H., et al. (2022). Embryo model completes gastrulation to neurulation and organogenesis. *Nature* **610**, 143–153. <https://doi.org/10.1038/s41586-022-05246-3>.
12. Lau, K.Y.C., Rubinstein, H., Gantner, C.W., Hadas, R., Amadei, G., Stelzer, Y., and Zernicka-Goetz, M. (2022). Mouse embryo model derived exclusively from embryonic stem cells undergoes neurulation and heart development. *Cell Stem Cell* **29**, 1445–1458.e8. <https://doi.org/10.1016/j.stem.2022.08.013>.
13. Stevens, A.J., Harris, A.R., Gerdts, J., Kim, K.H., Trentesaux, C., Ramirez, J.T., McKeithan, W.L., Fattah, F., Klein, O.D., Fletcher, D.A., et al. (2023). Programming multicellular assembly with synthetic cell adhesion molecules. *Nature* **614**, 144–152. <https://doi.org/10.1038/s41586-022-05622-z>.
14. Fots, R.A., and Steinberg, M.S. (2005). The differential adhesion hypothesis: a direct evaluation. *Dev. Biol.* **278**, 255–263. <https://doi.org/10.1016/j.ydbio.2004.11.012>.
15. Fridy, P.C., Li, Y., Keegan, S., Thompson, M.K., Nudelman, I., Scheid, J.F., Oeffinger, M., Nussenzweig, M.C., Fenyö, D., Chait, B.T., et al. (2014). A robust pipeline for rapid production of versatile nanobody repertoires. *Nat. Methods* **11**, 1253–1260. <https://doi.org/10.1038/nmeth.3170>.
16. Ferrer-Vaquer, A., Piliszek, A., Tian, G., Aho, R.J., Dufort, D., and Hadjantonakis, A.-K. (2010). A sensitive and bright single-cell resolution live imaging reporter of Wnt/β-catenin signaling in the mouse. *BMC Dev. Biol.* **10**, 121. <https://doi.org/10.1186/1471-213X-10-121>.
17. Turner, D.A., Girgin, M., Alonso-Crisostomo, L., Trivedi, V., Baillie-Johnson, P., Glodowski, C.R., Hayward, P.C., Collignon, J., Gustavsen, C., Serup, P., et al. (2017). Anteroposterior polarity and elongation in the absence of extra-embryonic tissues and of spatially localised signalling in gastruloids: mammalian embryonic organoids. *Development* **144**, 3894–3906. <https://doi.org/10.1242/dev.150391>.
18. Gossen, M., Freundlieb, S., Bender, G., Müller, G., Hillen, W., and Bujard, H. (1995). Transcriptional Activation by Tetracyclines in Mammalian Cells. *Science* **268**, 1766–1769. <https://doi.org/10.1126/science.7792603>.
19. Li, Q., Vlachos, E.N., and Bryant, P. (2024). Design of linear and cyclic peptide binders of different lengths only from a protein target sequence. Preprint at bioRxiv. <https://doi.org/10.1101/2024.06.20.599739>.
20. Soliman, S.S., Shah, D.H., El-Samad, H., and Weinberg, Z.Y. (2024). Small molecule and cell contact-inducible systems for controlling expression and differentiation in stem cells. Preprint at bioRxiv. <https://doi.org/10.1101/2024.03.12.584464>.
21. Tague, E.P., Dotson, H.L., Tunney, S.N., Sloas, D.C., and Ngo, J.T. (2018). Chemogenetic control of gene expression and cell signaling with antiviral drugs. *Nat. Methods* **15**, 519–522. <https://doi.org/10.1038/s41592-018-0042-y>.
22. Gargett, T., and Brown, M.P. (2014). The inducible caspase-9 suicide gene system as a “safety switch” to limit on-target, off-tumor toxicities of chimeric antigen receptor T cells. *Front. Pharmacol.* **5**, 235. <https://doi.org/10.3389/fphar.2014.00235>.
23. Gadue, P., Huber, T.L., Paddison, P.J., and Keller, G.M. (2006). Wnt and TGF-β signaling are required for the induction of an in vitro model of primitive streak formation using embryonic stem cells. *Proc. Natl. Acad. Sci. USA* **103**, 16806–16811. <https://doi.org/10.1073/pnas.0603916103>.
24. van den Brink, S.C., Baillie-Johnson, P., Balayo, T., Hadjantonakis, A.-K., Nowotschin, S., Turner, D.A., and Martinez Arias, A. (2014). Symmetry breaking, germ layer specification and axial organisation in aggregates of mouse embryonic stem cells. *Development* **141**, 4231–4242. <https://doi.org/10.1242/dev.113001>.
25. Wang, J., Sinha, T., and Wynshaw-Boris, A. (2012). Wnt Signaling in Mammalian Development: Lessons from Mouse Genetics. *Cold Spring Harb. Perspect. Biol.* **4**, a007963. <https://doi.org/10.1101/cshperspect.a007963>.
26. Beccari, L., Moris, N., Girgin, M., Turner, D.A., Baillie-Johnson, P., Cossy, A.-C., Lutolf, M.P., Duboule, D., and Arias, A.M. (2018). Multi-axial self-organization properties of mouse embryonic stem cells into gastruloids. *Nature* **562**, 272–276. <https://doi.org/10.1038/s41586-018-0578-0>.
27. Deluz, C., Friman, E.T., Strebinger, D., Benke, A., Raccaud, M., Callegari, A., Leleu, M., Manley, S., and Suter, D.M. (2016). A role for mitotic book-marking of SOX2 in pluripotency and differentiation. *Genes Dev.* **30**, 2538–2550. <https://doi.org/10.1101/gad.289256.116>.
28. McNamara, H.M., Solley, S.C., Adamson, B., Chan, M.M., and Toettcher, J.E. (2023). Recording morphogen signals reveals origins of gastruloid symmetry breaking. Preprint at bioRxiv. <https://doi.org/10.1101/2023.06.02.543474>.
29. Morgani, S.M., Metzger, J.J., Nichols, J., Siggia, E.D., and Hadjantonakis, A.-K. (2018). Micropattern differentiation of mouse pluripotent stem cells

- recapitulates embryo regionalized cell fate patterning. *eLife* 7, e32839. <https://doi.org/10.7554/eLife.32839>.
30. Amin, S., Neijts, R., Simmuni, S., van Rooijen, C., Tan, S.C., Kester, L., van Oudenaarden, A., Creyghton, M.P., and Deschamps, J. (2016). Cdx and T Brachyury Co-activate Growth Signaling in the Embryonic Axial Progenitor Niche. *Cell Rep.* 17, 3165–3177. <https://doi.org/10.1016/j.celrep.2016.11.069>.
31. Foley, T.E., Hess, B., Savory, J.G.A., Ringuelette, R., and Lohnes, D. (2019). Role of Cdx factors in early mesodermal fate decisions. *Development* 146, dev170498. <https://doi.org/10.1242/dev.170498>.
32. Bardot, E., Calderon, D., Santoriello, F., Han, S., Cheung, K., Jadhav, B., Burtscher, I., Artap, S., Jain, R., Epstein, J., et al. (2017). Foxa2 identifies a cardiac progenitor population with ventricular differentiation potential. *Nat. Commun.* 8, 14428. <https://doi.org/10.1038/ncomms14428>.
33. Rivera-Pérez, J.A., and Magnuson, T. (2005). Primitive streak formation in mice is preceded by localized activation of *Brachyury* and *Wnt3*. *Dev. Biol.* 288, 363–371. <https://doi.org/10.1016/j.ydbio.2005.09.012>.
34. Zhang, S., and Cui, W. (2014). Sox2, a key factor in the regulation of pluripotency and neural differentiation. *World J. Stem Cells* 6, 305–311. <https://doi.org/10.4252/wjst.v6.i3.305>.
35. Funakoshi, S., Fernandes, I., Mastikhina, O., Wilkinson, D., Tran, T., Dhahri, W., Mazine, A., Yang, D., Burnett, B., Lee, J., et al. (2021). Generation of mature compact ventricular cardiomyocytes from human pluripotent stem cells. *Nat. Commun.* 12, 3155. <https://doi.org/10.1038/s41467-021-23329-z>.
36. Acampora, D., Di Giovannantonio, L.G., and Simeone, A. (2013). Otx2 is an intrinsic determinant of the embryonic stem cell state and is required for transition to a stable epiblast stem cell condition. *Development* 140, 43–55. <https://doi.org/10.1242/dev.085290>.
37. Vernay, B., Koch, M., Vaccarino, F., Briscoe, J., Simeone, A., Kageyama, R., and Ang, S.-L. (2005). Otx2 Regulates Subtype Specification and Neurogenesis in the Midbrain. *J. Neurosci.* 25, 4856–4867. <https://doi.org/10.1523/JNEUROSCI.5158-04.2005>.
38. Wilson, P.G., and Stice, S.S. (2006). Development and differentiation of neural rosettes derived from human embryonic stem cells. *Stem Cell Rev.* 2, 67–77. <https://doi.org/10.1007/s12055-006-0011-1>.
39. Pijuan-Sala, B., Griffiths, J.A., Guibentif, C., Hiscock, T.W., Jawaid, W., Calero-Nieto, F.J., Mulas, C., Ibarra-Soria, X., Tyser, R.C.V., Ho, D.L.L., et al. (2019). A single-cell molecular map of mouse gastrulation and early organogenesis. *Nature* 566, 490–495. <https://doi.org/10.1038/s41586-019-0933-9>.
40. Kubo, A., Shinozaki, K., Shannon, J.M., Kouskoff, V., Kennedy, M., Woo, S., Fehling, H.J., and Keller, G. (2004). Development of definitive endoderm from embryonic stem cells in culture. *Development* 131, 1651–1662. <https://doi.org/10.1242/dev.01044>.
41. Zorn, A.M., and Wells, J.M. (2009). Vertebrate Endoderm Development and Organ Formation. *Annu. Rev. Cell Dev. Biol.* 25, 221–251. <https://doi.org/10.1146/annurev.cellbio.042308.113344>.
42. Yokomizo, T., Takahashi, S., Mochizuki, N., Kuroha, T., Ema, M., Wakamatsu, A., Shimizu, R., Ohneda, O., Osato, M., Okada, H., et al. (2007). Characterization of GATA-1<sup>+</sup> hemangioblastic cells in the mouse embryo. *EMBO J.* 26, 184–196. <https://doi.org/10.1038/sj.emboj.7601480>.
43. Murakami, K., Günesdogan, U., Zyllicz, J.J., Tang, W.W.C., SenGupta, R., Kobayashi, T., Kim, S., Butler, R., Dietmann, S., and Surani, M.A. (2016). NANOG alone induces germ cells in primed epiblast in vitro by activation of enhancers. *Nature* 529, 403–407. <https://doi.org/10.1038/nature16480>.
44. Yao, C., Yao, R., Luo, H., and Shuai, L. (2022). Germline specification from pluripotent stem cells. *Stem Cell Res. Ther.* 13, 74. <https://doi.org/10.1186/s13287-022-02750-1>.
45. Jakobsson, L., Franco, C.A., Bentley, K., Collins, R.T., Ponsioen, B., Aspalter, I.M., Rosewell, I., Busse, M., Thurston, G., Medvinsky, A., et al. (2010). Endothelial cells dynamically compete for the tip cell position during angiogenic sprouting. *Nat. Cell Biol.* 12, 943–953. <https://doi.org/10.1038/ncb2103>.
46. Rossi, G., Broguiere, N., Miyamoto, M., Boni, A., Quiet, R., Girgin, M., Kelly, R.G., Kwon, C., and Lutolf, M.P. (2021). Capturing Cardiogenesis in Gastruloids. *Cell Stem Cell* 28, 230–240.e6. <https://doi.org/10.1016/j.stem.2020.10.013>.
47. Giacomelli, E., Meraviglia, V., Camponstri, G., Cochrane, A., Cao, X., van Helden, R.W.J., Krotenberg Garcia, A., Mircea, M., Kostidis, S., Davis, R.P., et al. (2020). Human-iPSC-Derived Cardiac Stromal Cells Enhance Maturation in 3D Cardiac Microtissues and Reveal Non-cardiomyocyte Contributions to Heart Disease. *Cell Stem Cell* 26, 862–879.e11. <https://doi.org/10.1016/j.stem.2020.05.004>.
48. Thomas, D., Choi, S., Alamana, C., Parker, K.K., and Wu, J.C. (2022). Cellular and Engineered Organoids for Cardiovascular Models. *Circ. Res.* 130, 1780–1802. <https://doi.org/10.1161/CIRCRESAHA.122.320305>.
49. Marvin, M.J., Di Rocco, G.D., Gardiner, A., Bush, S.M., and Lassar, A.B. (2001). Inhibition of Wnt activity induces heart formation from posterior mesoderm. *Genes Dev.* 15, 316–327. <https://doi.org/10.1101/gad.855501>.
50. Schultheiss, T.M., Burch, J.B., and Lassar, A.B. (1997). A role for bone morphogenetic proteins in the induction of cardiac myogenesis. *Genes Dev.* 11, 451–462. <https://doi.org/10.1101/gad.11.4.451>.
51. Hofbauer, P., Jahn, S.M., Papai, N., Giesshammer, M., Deyett, A., Schmidt, C., Penc, M., Tavernini, K., Grdseloff, N., Meledeth, C., et al. (2021). Cardioids reveal self-organizing principles of human cardiogenesis. *Cell* 184, 3299–3317.e22. <https://doi.org/10.1016/j.cell.2021.04.034>.
52. Steinberg, M.S. (1963). Reconstruction of Tissues by Dissociated Cells. Some morphogenetic tissue movements and the sorting out of embryonic cells may have a common explanation. *Science* 141, 401–408. <https://doi.org/10.1126/science.141.3579.401>.
53. Cederquist, G.Y., Asciola, J.J., Tchieu, J., Walsh, R.M., Cornacchia, D., Resh, M.D., and Studer, L. (2019). Specification of positional identity in forebrain organoids. *Nat. Biotechnol.* 37, 436–444. <https://doi.org/10.1038/s41587-019-0085-3>.
54. Xu, P.-F., Borges, R.M., Fillatre, J., de Oliveira-Melo, M., Cheng, T., Thisse, B., and Thisse, C. (2021). Construction of a mammalian embryo model from stem cells organized by a morphogen signalling centre. *Nat. Commun.* 12, 3277. <https://doi.org/10.1038/s41467-021-23653-4>.
55. Arias, A.M., Marikawa, Y., and Moris, N. (2022). Gastruloids: Pluripotent stem cell models of mammalian gastrulation and embryo engineering. *Dev. Biol.* 488, 35–46. <https://doi.org/10.1016/j.ydbio.2022.05.002>.
56. Zernicka-Goetz, M. (2023). The evolution of embryo models. *Nat. Methods* 20, 1844–1848. <https://doi.org/10.1038/s41592-023-02077-6>.
57. Brassard, J.A., Nikolaev, M., Hübscher, T., Hofer, M., and Lutolf, M.P. (2021). Recapitulating macro-scale tissue self-organization through organoid bioprinting. *Nat. Mater.* 20, 22–29. <https://doi.org/10.1038/s41563-020-00803-5>.
58. Elowitz, M., and Lim, W.A. (2010). Build life to understand it. *Nature* 468, 889–890. <https://doi.org/10.1038/468889a>.
59. Lim, W.A. (2022). The emerging era of cell engineering: Harnessing the modularity of cells to program complex biological function. *Science* 378, 848–852. <https://doi.org/10.1126/science.add9665>.
60. Longo, S.K., Guo, M.G., Ji, A.L., and Khavari, P.A. (2021). Integrating single-cell and spatial transcriptomics to elucidate intercellular tissue dynamics. *Nat. Rev. Genet.* 22, 627–644. <https://doi.org/10.1038/s41576-021-00370-8>.
61. Moses, L., and Pachter, L. (2022). Museum of spatial transcriptomics. *Nat. Methods* 19, 534–546. <https://doi.org/10.1038/s41592-022-01409-2>.
62. Tian, L., Chen, F., and Macosko, E.Z. (2023). The expanding vistas of spatial transcriptomics. *Nat. Biotechnol.* 41, 773–782. <https://doi.org/10.1038/s41587-022-01448-2>.
63. Zeng, H., Huang, J., Ren, J., Wang, C.K., Tang, Z., Zhou, H., Zhou, Y., Shi, H., Aditham, A., Sui, X., et al. (2023). Spatially resolved single-cell

- translatomics at molecular resolution. *Science* 380, eadd3067. <https://doi.org/10.1126/science.add3067>.
64. Baron, C.S., and van Oudenaarden, A. (2019). Unravelling cellular relationships during development and regeneration using genetic lineage tracing. *Nat. Rev. Mol. Cell Biol.* 20, 753–765. <https://doi.org/10.1038/s41580-019-0186-3>.
65. Bergen, V., Lange, M., Peidli, S., Wolf, F.A., and Theis, F.J. (2020). Generalizing RNA velocity to transient cell states through dynamical modeling. *Nat. Biotechnol.* 38, 1408–1414. <https://doi.org/10.1038/s41587-020-0591-3>.
66. Chen, Z., King, W.C., Hwang, A., Gerstein, M., and Zhang, J. (2022). Deep-Velo: Single-cell transcriptomic deep velocity field learning with neural ordinary differential equations. *Sci. Adv.* 8, eabq3745. <https://doi.org/10.1126/sciadv.abq3745>.
67. VanHorn, S., and Morris, S.A. (2021). Next-Generation Lineage Tracing and Fate Mapping to Interrogate Development. *Dev. Cell* 56, 7–21. <https://doi.org/10.1016/j.devcel.2020.10.021>.
68. Wagner, D.E., and Klein, A.M. (2020). Lineage tracing meets single-cell omics: opportunities and challenges. *Nat. Rev. Genet.* 21, 410–427. <https://doi.org/10.1038/s41576-020-0223-2>.
69. Tarazi, S., Aguilera-Castrejon, A., Joubran, C., Ghanem, N., Ashouokhi, S., Roncato, F., Wildschut, E., Haddad, M., Oldak, B., Gomez-Cesar, E., et al. (2022). Post-gastrulation synthetic embryos generated ex utero from mouse naive ESCs. *Cell* 185, 3290–3306.e25. <https://doi.org/10.1016/j.cell.2022.07.028>.
70. Liberali, P., and Schier, A.F. (2024). The evolution of developmental biology through conceptual and technological revolutions. *Cell* 187, 3461–3495. <https://doi.org/10.1016/j.cell.2024.05.053>.
71. Martínez-Ara, G., Stapornwongkul, K.S., and Ebisuya, M. (2022). Scaling up complexity in synthetic developmental biology. *Science* 378, 864–868. <https://doi.org/10.1126/science.add9666>.
72. McNamara, H.M., Ramm, B., and Toettcher, J.E. (2023). Synthetic developmental biology: New tools to deconstruct and rebuild developmental systems. *Semin. Cell Dev. Biol.* 141, 33–42. <https://doi.org/10.1016/j.semcdb.2022.04.013>.
73. Berg, S., Kutra, D., Kroeger, T., Straehle, C.N., Kausler, B.X., Haubold, C., Schiegg, M., Ales, J., Beier, T., Rudy, M., et al. (2019). ilastik: interactive machine learning for (bio)image analysis. *Nat. Methods* 16, 1226–1232. <https://doi.org/10.1038/s41592-019-0582-9>.
74. Fonseca, J.P., Bonny, A.R., Kumar, G.R., Ng, A.H., Town, J., Wu, Q.C., Aslankoohi, E., Chen, S.Y., Dods, G., Harrigan, P., et al. (2019). A Toolkit for Rapid Modular Construction of Biological Circuits in Mammalian Cells. *ACS Synth. Biol.* 8, 2593–2606. <https://doi.org/10.1021/acssynbio.9b00322>.
75. McGinnis, C.S., Patterson, D.M., Winkler, J., Conrad, D.N., Hein, M.Y., Srivastava, V., Hu, J.L., Murrow, L.M., Weissman, J.S., Werb, Z., et al. (2019). MULTI-seq: sample multiplexing for single-cell RNA sequencing using lipid-tagged indices. *Nat. Methods* 16, 619–626. <https://doi.org/10.1038/s41592-019-0433-8>.

## STAR★METHODS

## KEY RESOURCES TABLE

REAGENT or RESOURCE	SOURCE	IDENTIFIER
<b>Antibodies</b>		
Rat monoclonal anti-P-cadherin	Thermo Fisher Scientific	Cat# 13-2000Z; RRID: AB_2533006
Rabbit polyclonal anti-N-cadherin	Abcam	Cat# ab76057; RRID: AB_1310478
Rabbit polyclonal anti-K-cadherin	GeneTex	Cat# GTX3279; RRID: AB_2887705
Goat polyclonal anti-Nkx2.5	Santa Cruz Biotechnology	Cat# sc-8697; RRID: AB_650280
Mouse monoclonal anti-cTnT	Thermo Fisher Scientific	Cat# MA5-12960; RRID: AB_11000742
Rat monoclonal anti-Pecam1	Thermo Fisher Scientific	Cat# BDB553370; RRID: AB_396660
Rabbit monoclonal anti-Brachury	Abcam	Cat# ab209665; RRID: AB_2750925
Mouse monoclonal anti-Cdx2	Abcam	Cat# ab157524; RRID: AB_2721036
Rabbit monoclonal anti-FoxA2	Cell Signaling Technology	Cat# 8186S; RRID: AB_10891055
Rat monoclonal anti-Sox2	Thermo Fisher Scientific	Cat# 14-9811-82; RRID: AB_11219471
Goat polyclonal anti-Sox17	R&D Systems	Cat# AF1924; RRID: AB_355060
Rat monoclonal anti-Gata1	Santa Cruz Biotechnology	Cat# sc-265; RRID: AB_627663
Rabbit monoclonal anti-Runx1/2/3	Abcam	Cat# ab92336; RRID: AB_2049267
Rat monoclonal anti-Blimp1 (Prdm1)	Thermo Fisher Scientific	Cat# 14-5963-82; RRID: AB_1907437
Mouse polyclonal anti-Nanog	StemAb	Cat# RCAB002P-F; RRID: AB_2616320
Goat polyclonal anti-Otx2	R&D System	Cat# AF1979; RRID: AB_215717
Rabbit monoclonal anti-beta 3 Tubulin	Abcam	Cat# ab52623; RRID: AB_869991
Donkey anti-rat Alexa Fluor 488	Thermo Fisher Scientific	Cat# A-21208; RRID: AB_2535794
Donkey anti-goat Alexa Fluor 488	Thermo Fisher Scientific	Cat# A-11055; RRID: AB_2534102
Goat anti-rabbit Alexa Fluor 488	Thermo Fisher Scientific	Cat# A-11008; RRID: AB_143165
Donkey anti-mouse Alexa Fluor 568	Thermo Fisher Scientific	Cat# A-10037; RRID: AB_2534013
RNAscope Probe-Mm-Bmp4-C1	ACD Bio	Cat# 401301
<b>Bacterial and virus strains</b>		
Stbl3 competent cells	Macro lab	N/A
<b>Chemicals, peptides, and recombinant proteins</b>		
DMEM/F-12, GlutaMAX supplement	Thermo Fisher Scientific	10-565-042
Neurobasal Medium	Thermo Fisher Scientific	21103049
B-27 Supplement (50X)	Thermo Fisher Scientific	12587010
N-2 Supplement (100X)	Thermo Fisher Scientific	17502048
DMEM, high glucose, GlutaMAX Supplement, HEPES	Thermo Fisher Scientific	10-564-029
Penicillin-streptomycin	Thermo Fisher Scientific	151140-122
FBS	UCSF Cell Culture Facility	CCFAQ008
FBS, embryonic stem cell-qualified	Thermo Fisher Scientific	10439024
0.1% Gelatin in water	Stem Cell Technologies	07903
2-Mercaptoethanol	Thermo Fisher Scientific	21985-023
MEM Non-Essential Amino Acid (NEAA)	Thermo Fisher Scientific	11140-050
Sodium Pyruvate	Thermo Fisher Scientific	11360-070
GlutaMAX	Thermo Fisher Scientific	35050-061
TransIT-VirusGEN	Mirus Bio	MIR 6706
Puromycin	Thermo Fisher Scientific	A11138-03
Hygromycin B	Thermo Fisher Scientific	10687010
TrypLe	Thermo Fisher Scientific	12604-013
ESGRO mLIF supplement	Millipore	3769655

(Continued on next page)

**Continued**

REAGENT or RESOURCE	SOURCE	IDENTIFIER
CHIR99021	Stem Cell Technologies	72054
PD0325901	Stem Cell Technologies	72184
Recombinant murine Wnt3a	PeproTech	315-20
Phalloidin-iFluor 488	Abcam	Ab176753
DRAQ5	BioLegend	424101
TO-PRO3	Thermo Fisher Scientific	T3605
Fluo-4, AM, cell permeant	Thermo Fisher Scientific	F14217
Doxycycline hydrochloride	Sigma-Aldrich	D3447
Grazoprevir	MedChemExpress	HY-15298
LDN-193189	Stemgent	04-0074-10
AP20187	Sigma	SML2838-1MG
Formalin solution, neutral buffered, 10%	Sigma-Aldrich	HT5012-1CS
RNAscope Multiplex Fluorescent Reagent Kit v2	ACD Bio	323110

**Deposited data**

scRNA-seq Day 8 using Wnt3a node	This study	GEO: GSE244033
scRNA-seq Day8 using Dkk1 node	This study	GEO: GSE244033
scRNA-seq Day8 using Wnt3a node and Dkk1 node	This study	GEO: GSE244033
Bulk RNA-seq of Wnt3a node	This study	GEO: GSE244033
Bulk RNA-seq of Dkk1 node	This study	GEO: GSE244033
scRNA-seq of E6.5 to E8.5 mouse embryo	Pijuan-Sala et al. <sup>39</sup>	ArrayExpress: E-MTAB-6967
scRNA-seq of cardiac gastruloid	Rossi <sup>46</sup>	GEO: GSE158999

**Experimental models: Cell lines**

Mouse: TCF-mCherry reporter mESC expressing nfGFP-ligand and H2B-670	This study	Origin: E14Tg2a
Mouse: Brachury-mCherry::Sox1-EGFP reporter mESC expressing nfGFP-ligand and H2B-iRFP670	This study	Origin: CGR8, strain 129
Mouse: Kdr-EGFP reporter mESC expressing nfGFP-ligand and H2B-iRFP670	This study	Origin: E14Tg2a
Mouse: mESC expressing nfGFP-ligand and H2B-iRFP670	This study	Origin: E14Tg2a
Mouse: WNT3 node (L929)	This study	N/A
Mouse: WNT3A node with suicide switch (L929)	This study	N/A
Mouse: Activin A node (L929)	This study	N/A
Mouse: Dkk1 node (L929)	This study	N/A
Mouse: Wnt3a shell (L929)	This study	N/A
Mouse: Dkk1 shell (L929)	This study	N/A
Mouse: L929 cells expressing K-cad	This study	N/A
Mouse: L929 cells expressing N-cad	This study	N/A
Mouse: L929 cells expressing P-cad	This study	N/A
Mouse: L929 cells expressing Lag16-tether	This study	N/A
Mouse: L929 cells expressing Lag16-DLL	This study	N/A
Mouse: L929 cells expressing Lag16-ICAM1	This study	N/A
Mouse: L929 cells expressing Lag16-ECAD	This study	N/A
Mouse: L929 cells expressing Lag16-ITGB1	This study	N/A
Mouse: L929 cells expressing Lag16-ITGB2	This study	N/A

(Continued on next page)

**Continued**

REAGENT or RESOURCE	SOURCE	IDENTIFIER
Human: Lenti-X™ 293T cell Line	Takara Bio	Cat#632180
<b>Recombinant DNA</b>		
pPGK1-Pcad-IRES-PuroR-WPRE	This study	Addgene: 225348
pEF1a-TetOn3G_pPGK1-HygroR-WPRE	This study	N/A
pTRE-Wnt3a-IRES-tagBFP2-WPRE	This study	Addgene: 225349
pTRE-ActivinA-IRES-tagBFP2-WPRE	This study	Addgene: 225355
pCAG_nfGFP-tether-P2A-H2B-iRFP670-SV40	This study	Addgene: 225350
pEF1a-VP64-NS3-Gal4-DBD_pPGK1-HygroR-WPRE	This study	N/A
pEF1a-iCasp9-P2A-mNeonGreen-WPRE	This study	N/A
pUAS-Dkk1-IRES-tagBFP2-WPRE	This study	Addgene: 225353
pPGK1-mTagBFP2-WPRE	This study	Addgene: 225352
pPGK1-iRFP670-WPRE	This study	Addgene: 225351
pPGK1-Kcad-IRES-PuroR-WPRE	This study	Addgene: 225347
pPGK1-Ncad-IRES-PuroR-WPRE	This study	Addgene: 225354
pPGK1-Lag16-ITGB2-WPRE	Stevens et al. <sup>13</sup>	Addgene: 205203
pPGK1-Lag16-ICAM1-WPRE	Stevens et al. <sup>13</sup>	Addgene: 205195
pPGK1-Lag16-tether-WPRE	Stevens et al. <sup>13</sup>	Addgene: 205196
pPGK1-Lag16-DLL-WPRE	Stevens et al. <sup>13</sup>	Addgene: 205201
pPGK1-Lag16-ECAD-WPRE	Stevens et al. <sup>13</sup>	Addgene: 205197
<b>Software and algorithms</b>		
Fiji	NIH Image	<a href="https://imagej.nih.gov/ij/">https://imagej.nih.gov/ij/</a>
MATLAB	MathWorks	<a href="https://www.mathworks.com/?s_tid=gn_logo">https://www.mathworks.com/?s_tid=gn_logo</a>
Ilastik	Berg <sup>73</sup>	–
Original codes	This study	Zenodo: 12642864 ( <a href="https://zenodo.org/doi/10.5281/zenodo.12642864">https://zenodo.org/doi/10.5281/zenodo.12642864</a> )
<b>Other</b>		
96-well Clear Round Bottom Ultra-Low Attachment Microplate	Corning	7007
μ-Slide 8 Well	Ibidi	80806
μ-Slide 18 Well	Ibidi	81816
Nexcelom3D 384-well Ultra-low attachment treated round bottom multi-well plates	Nexcelom Bioscience	ULA-384U-520

**EXPERIMENTAL MODEL AND SUBJECT DETAILS****Cell lines and culture conditions**

We have used the following ESC lines:

- pTCF-mCherry reporter mESCs with membrane nfGFP and H2B-iRFP670 expression, generated by piggyBac transposon.
- Brachury-mCherry::Sox1-EGFP reporter mESCs with membrane nfGFP and H2B-iRFP670 expression, generated by piggyBac transposon.
- Kdr-EGFP reporter mESCs with membrane nfGFP and H2B-iRFP670 expression, generated by piggyBac transposon.
- WT mESCs (E14Tg2a) with membrane nfGFP and H2B-iRFP670 expression, generated by piggyBac transposon.

Also, we have generated the following synthetic organizer cells:

- Wnt3a node: L929 cells expressing P-cad and Lag16-ICAM1 with overexpressing Wnt3a-IRES-tagBFP2 upon DOX induction, generated by Lenti-virus transduction.

- Wnt3a node with a suicide switch: Wnt3a node with expressing iCasp9, generated by Lenti-virus transduction.
- Wnt3a shell: L929 cells expressing Lag16-ITGB2 with overexpressing Wnt3a-IRES-tagBFP2 upon DOX induction, generated by Lenti-virus transduction.
- Dkk1 node: L929 cells expressing P-cad and Lag16-ICAM1, and iRFP670 with overexpressing Dkk1-IRES-tagBFP2 upon GRZ induction, generated by Lenti-virus transduction.
- Dkk1 shell: L929 cells expressing Lag16-ITGB2 and iRFP670 with overexpressing Dkk1-IRES-tagBFP2 upon GRZ induction, generated by Lenti-virus transduction.
- Activin A node: L929 cells expressing P-cad and Lag16-ICAM1 with overexpressing Activin A-IRES-tagBFP, generated by Lenti-virus transduction.
- L929 cells expressing P-cad and tagBFP2, generated by Lenti-virus transduction.
- L929 cells expressing K-cad and tagBFP2, generated by Lenti-virus transduction.
- L929 cells expressing N-cad and tagBFP2, generated by Lenti-virus transduction.
- L929 cells expressing Lag16-tether and tagBFP2, generated by Lenti-virus transduction.
- L929 cells expressing Lag16-DLL and tagBFP2, generated by Lenti-virus transduction.
- L929 cells expressing Lag16-ICAM1 and tagBFP2, generated by Lenti-virus transduction.
- L929 cells expressing Lag16-ECAD and tagBFP2, generated by Lenti-virus transduction.
- L929 cells expressing Lag16-ITGB1 and tagBFP2, generated by Lenti-virus transduction.
- L929 cells expressing Lag16-ITGB2 and tagBFP2, generated by Lenti-virus transduction.

mESCs were cultured at 37°C and 5% CO<sub>2</sub> in 2iLIF medium (DMEM + Glutamax (10564-011; Gibco) supplemented by 10% embryonic stem cell qualified FBS (Gibco), 0.1% 2-Mercaptoethanol (21985-023; Gibco), 1% MEM Non-Essential Amino Acid (NEAA) (11140-050; Gibco), and 1% Sodium Pyruvate (11360-070; Gibco), 3 μM CHIR99021 (Chir) (Stem Cell Technologies), 1 μM PD0305901 (Stem Cell Technologies), 0.01 μg/ml LIF (Stem Cell Technologies), and 1% penicillin-streptomycin (151140-122; Gibco)). Prior to plating mESCs, add 1 mL of 0.1% gelatin (07903; Stem Cell Technologies) to a 12-well plate and let sit at least for an 1 hr. Cells were passaged every other day with TrypLE Express (Gibco). If the cells were not being passaged, the media was replaced with fresh 2iLIF medium.

L929 cells were cultured in D10 medium (DMEM(1x) + Glutamax (10564-011; Gibco) supplemented by 10% FBS (89510; University of California, San Francisco [UCSF] Cell Culture Facility), and 1% penicillin-streptomycin (151140-122; Gibco)). Cells were cultured in a 37°C incubator at 5% CO<sub>2</sub> atmosphere.

## METHOD DETAILS

### Gene construction and cloning

All the plasmids were constructed by using the Mammalian Cloning Toolkit (MTK).<sup>74</sup> In brief, each element (promoter, coding region, 3'UTR) was introduced into the MTK system either by PCR or gene block (IDT). A library of circuit components was assembled into transcriptional units with a Bsal Golden Gate reaction. After bacterial transformation, plasmid DNAs were extracted (QIAprep Spin Miniprep Kit; 27106) and their sequence were verified. All plasmids are listed in the [key resources table](#) and will be available at Addgene or upon request. See [Table S2](#) for coding sequence of Wnt3a, Dkk1, and Activin A.

### Establishing synthetic organizer cell lines – lentivirus transduction

To generate synthetic organizer cells, we introduced our constructs to L929 cells using Lentivirus transduction. Lentivirus was produced using HEK293T lentiviral packaging cells (Takara bio, Cat# 632180) that were seeded in 6-well plates at 7x 10<sup>5</sup> cells/well and 24 hours later transfected with a pHRS lentiviral backbone and viral packaging plasmids pCMVdr8.91 and pMD2.g using TransIT-VirusGEN (22063557; Mirus) following the manufacturer's protocol. 48 hours after transfection viral supernatant was collected and passed through a 0.45 mm filter prior to use with L929 cells and used immediately for transduction. L929 cells were plated in a 12 well plate in 500 μL of 1.0x10<sup>5</sup> cells/mL and 500 μL of Lentiviral supernatant. 48 hours after infection, the virus media were removed, and cells were replaced with 1 mL of D10 medium. Cells were split if they reached approximately 80% confluence.

After Lentiviral transduction, positive cells were selected using Puromycin antibiotics (A11138-03; Gibco) or Hygromycin (10687010; Invitrogen). Positive cells were examined under the Opera Phenix with 5x air-immersion objective lens using brightfield and BFP channels. After the selection, single clonal cell line was selected by plating a single cell per well in 96-well plate. Phenotypes of each clone, such as morphologies and BFP expression level, were examined under the Opera Phenix with 5x air-immersion objective lens using brightfield and BFP channels.

### Establishing mESC lines - transduction plasmids using Nucleofection

Nucleofection is used to transduce plasmids into mESCs, employing the piggyBac transposon system. Plasmids were prepared by mixing 1 μg of piggyBac plasmid, 1 ug of transposase plasmid, 82 μL of nucleofector solution and 18 μL of supplement. Following the preparation of the master mix, mESCs are collected from their 12-well plate and detached using 300 μL of TrypLE (12604-013; Gibco). After waiting for 3-5 minutes, 1 mL of media was added, and the cells were transferred to a 15 ml conical tube. The cells

were spun down at 400g for 4 minutes. The supernatant was removed, and cells were resuspended in 1 mL of media. Cells were diluted to  $1 \times 10^5$  cells/mL. After spinning down the cells, the cells were resuspended with 110  $\mu$ L of the prepared plasmid mix and transfer to the P3 Primary cell 4D nucleofector X kits cuvette. Nucleofection was carried out using the Lonza 4D Nucleofector Core Unit with CG104 program. Subsequently, the cells were diluted with 1 mL of 2iLIF mESC media and plate into 2 wells of a 12 well plate (500  $\mu$ L each), followed by the addition of 500  $\mu$ L of 2iLIF mESC media. After the transduction, positive cells were selected based on sorting iRFP670 positive cells by fluorescence-activated cell sorting (FACS).

### Synthetic organizer architecture construction around a mESC core and morphogen induction

mESCs and L929 cells were detached from tissue culture plates with TypLE and collected with 2iLIF medium for mESC or D10 medium for L929. After Centrifugation at 500g for 3 minutes, the cells were washed once with N2B27 medium. N2B27 media is based on DMEM/F12 (1x) (11330-032; Gibco) and Nuerobasal Medium (21103-049; Gibco), supplemented by, 1% B27 supplement (50X)(12587-010; Gibco), 0.5% N2 supplement (100x) (17502-048; Gibco), 1% MEM Non-Essential Amino Acid (NEAA) (11140-050; Gibco), 1% Sodium Pyruvate (11260-070; Gibco), 0.5% Glutamax (35050-061; Gibco), 0.2% 2-Mercaptoethanol (21985-023; Gibco), and 1% penicillin-streptomycin (151140-122; Gibco). The cells were then resuspended in N2B27 medium, and the cell concentrations were determined. The cells were diluted to experimental amounts: 100-600 cells/well for mESC, 30-120 cells/well for Nodes, and 10-50 cells/well for shells, and 40  $\mu$ L/well of mESCs and synthetic organizer shells were plated into an ultra-low attachment round bottom 96 well plate (7007; Costar), or 40  $\mu$ L/well of synthetic organizer nodes were plated into an ultra-low attachment round bottom 384 well plate. The Plates were spun down at 500g for 1 minute and were kept in a 37°C incubator at 5% CO<sub>2</sub> atmosphere.

The following day, nodes were transferred to the 96-well plate with the mESCs, resulting in a total volume of 80  $\mu$ L (single node or single shell) or 120  $\mu$ L (2 nodes or node & shell) per well. To induce Wnt3a expression by the L929 organizer cells, 40  $\mu$ L of N2B27 medium containing doxycycline (D3447, Sigma) at a final concentration of 200 ng/mL was added to wells on day 1. To induce Dkk1 expression by the L929 cells, 40  $\mu$ L of N2B27 medium with grazoprevir (GRZ, MK-5172, MedChemExpress) at final concentration of 1.0 uM was added to wells on day 1. To activate suicide switch, N2B27 medium containing AP20187 at the final concertation of 1.0 uM was added to the wells. To inhibit BMP signaling, N2B27 medium containing LDN-193189 at the final concertation of 500 nM was added to the wells.

From day 4 onwards, the total volume in each well was maintained at 200  $\mu$ L. Half of the medium (100  $\mu$ L) were replaced daily with fresh N2B27 medium containing the appropriate small molecules to maintain constant drug concentrations.

### Generating Gastruloid

Gastruloids were generated as previously described.<sup>26</sup> Briefly, 100-400 mESCs (Sox1-GFP::Brachyury-mCherry line) were plated in 40  $\mu$ L N2B27 in 96-well Clear Round Bottom Ultra-Low Attachment Microplates (7007, Corning). After 48 h, 150  $\mu$ L of N2B27 containing 3  $\mu$ M CHIR were added to each well. After 72 h, medium was changed with 150  $\mu$ L N2B27 every 24 hour.

### Live imaging

Plates were imaged on the Perkin Elmer Opera Phenix High Content Screening System using 10x air objective (NA = 0.3) lens with 2-pixel binning. Images were captured sequentially in multi-stacks, five-channel mode. The detailed imaging conditions were as follows: tagBFP for 500 millisecond (ms) exposure time, EGFP (Sox1) for 400 ms, EGFP (Kdr) for 100 ms, mCherry (Brachyury) for 1200 ms, mCherry (pTCF) for 1500 ms, iRFP670 for 400 ms, bright-field for 100 ms. Laser powers were 50% for all wavelengths. Z-stacks were set up to start at -10.0  $\mu$ m with each plane 7.4  $\mu$ m apart, capturing 16 planes in total.

### Calcium imaging

Calcium transients were imaged in embryoids with beating phenotypes on day 8, stained with Fluo-4 AM (F14217, Thermo Fisher Scientific) using a confocal microscope (Nikon, T2). 1  $\mu$ M Fluo-4 AM was added to the samples and incubated for at least 30 minutes. Then, the samples were washed twice with N2B27 medium and transferred to a  $\mu$ -slide 8 well (ibidi). Using a 20x Air objective lens, several 10 seconds recordings were acquired for each sample at a frame rate of 10 frames per second. Fluorescence intensities were quantified with Fiji software to measure the signal intensity (F) and background (F0).

### Immunostaining

Three to six samples were transferred to a new U-bottom 96 well plate (7007, Corning) using a p200 pipette with the tip cut-off at the 50  $\mu$ L position. The collected samples were washed once in PBS and then fixed in 10% neutral buffered formalin solution for overnight at 4°C. After fixation, the sample were washed twice with PBS and stored in PBS until staining was performed. the samples were permeabilized by three 20 minutes incubation in 1.0% Triton-X/PBS and blocked in Universal Blocking Solution (UBS: 1.0 g/dL BSA, 0.2 g/dL evaporated nonfat milk, 0.5% Triton X-100, 1% DMSO in PBS) for 1 hour at room temperature. Primary antibodies were incubated in UBS for 48-72 hours at 4C. Subsequently, the samples were washed three times with PBS with 0.1% Tween20 for 10 minutes at room temperature. Afterward, secondary antibodies and DRAQ5 or TO-PRO-3 (at a 500-fold dilution) diluted in UBS were incubated for 24-48 hours at 4C. Samples were then washed three times with PBS with 0.1% Tween20 and transferred

to  $\mu$ -slide 8 well or 18 well ibiTreat slide. In  $\mu$ -slide, samples were tissue cleared using 50% CUBIC-R+(M) (2-time dilution with water) for 1-4 hours in room temperature. All primary and secondary antibodies are listed in the [key resources table](#).

### Whole mount RNAscope staining

Samples were transferred to U-bottom 96 well plate. The collected samples were washed once in PBS and then fixed in 10% neutral buffered formalin solution overnight at 4°C. After fixation, samples were washed twice with PBS followed by dehydration in a graded methanol/PBS series (50%, 75%, 100%) for 5 min each at room temperature. The dehydrated samples were stored in 100% MeOH at – 25°C.

For the staining, the samples were re-hydrated in a reverse methanol/PBS series. The samples were then treated with 15-fold diluted Protease III solution for 10 min at room temperature. After three washes with PBS, the samples were incubated with RNA probe at 40 °C with light agitation (typically, 300 rpm). The samples were then washed three times with Wash buffer.

The Sample were then incubated with Amp1 pre-amplifier hybridization for 30 min at 40 °C. After washing with Wash buffer twice, the samples were incubated with Amp2 signal enhancement solution for 30 min at 40 °C. The samples were washed twice with Wash buffer and then incubated with Amp3 amplifier hybridization solution for 15 min at 40 °C. After washing with Wash buffer twice, the samples were incubated with HRP-C1 for 15 min at 40 °C. After washing with Wash buffer twice, the samples were incubated with Cy3 dyes (1:500 dilution) for 30 min at 40 °C. Following the Cy3 incubation, the samples were washed twice with Wash buffer and incubated with HRP-blocker for 15 minutes at 40°C. Finally, the samples were washed three times with Wash buffer.

Following the RNAscope protocol, samples were kept in UBS to perform immunostaining.

### Imaging fixed samples

Immunostained samples were imaged at the UCSF Nikon Imaging Center using a Nikon Ti2-E microscope equipped with Crest L-FOV spinning disk and C2 confocal with DUVb detector (Crest/C2). Images that capture an entire sample were taken with Crest spinning disk confocal using 10x Air (NA= 0.45) objective lens. For the detailed image around a chamber, embryonic blood clusters, PGC clusters, and OTX2-positive domains, C2 point-scanning confocal with 10xAir (NA= 0.45) objective lens was used.

### MULTI-seq sample preparation

Individual embryoids were labeled with unique lipid-modified oligonucleotide (LMOs) to multiplex multiple samples for MULTI-seq.<sup>75</sup> In brief, around 10 embryoids in each condition were transferred to a 96-well U-bottom plate and were digested using TrypLE. The cells were then washed with BGJb medium and labeled with 10  $\mu$ L of 2.5  $\mu$ M anchor LMO-barcode for 5 min on ice. Then, 10  $\mu$ L of 2.5  $\mu$ M co-anchor LMO were added to each cell pool, and samples were labeled for another 5 min on ice. Following LMO labeling, cells were washed with 1% BSA in PBS to quench LMOs. After washing, the cells were resuspended in FACS buffer with DAPI and live embryoid cells were sorted using BD FACS Aria. L929 node cells were sorted separately and mixed with embryoid cells at a 2% ratio. Transcripts of each cell were barcoded with 10 $\times$  Genomics Chromium system at the UCSF 10x Genomic core. Sequencing was carried out at the UCSF sequencing core with an Illumina NovaSeq X machine.

### scRNA-seq processing, clustering, and plotting of data

Sequencing reads were aligned using CellRanger version 7.0.0 (10x Genomics) to the mouse GRCm38.100 reference. Valid cells were identified with DropletUtils (<https://doi.org/10.1186/s13059-019-1662-y>). Demultiplexing and removal of predicted doublets and unclassified cells was done with the deMULTIplex2 R package (<https://doi.org/10.1101/2023.04.11.536275>) on MultiSeq barcode reads aligned with Multiseq10x (GitHub - Mignot-Lab/Multiseq10x). All further processing was done in Seurat V4 (<https://doi.org/10.1016/j.cell.2021.04.048>). Identified and demultiplexed cells were filtered according to number of UMIs per cell, number of genes per cell, and percentage of mitochondrial gene reads per cell. Each dataset was processed individually using the following pipeline of Seurat functions using default parameters and the first 50 principal components: SCTransform, RunPCA, FindNeighbors, FindClusters, RunUMAP. All datasets were annotated by assigning cell type identities based on marker gene expression identified using the FindAllMarkers function; the expression of key markers genes was visualized using dot plots.

To compare cell type annotations across datasets, we downsampled the WNT and Dual Node datasets to the same number of cells in the DKK dataset, then reprocessed and annotated the downsampled datasets using the pipeline described above. Downsampling, processing, and annotation was performed twice to ensure reproducibility of annotations obtained after random downsampling of cells.

To visualize all data on a common UMAP, we integrated the three datasets using fastMNN (<https://doi.org/10.1038/nbt.4091>) and then computed the UMAP using the top 50 MNN components identified by fastMNN as low-dimensional components.

### Comparison of cell types from organized embryoids with cell types from natural mouse embryos and gastruloids

Single cell gene expression and annotation data for natural mouse embryos were obtained using the R Bioconductor package MouseGastrulationData and removing doublets and cytoplasm-stripped nuclei; data for gastruloids were from GEO accession number GSE158999. These data were integrated with the single WNT node, single DKK node, and dual WNT/DKK1 nodes datasets using the R package cFIT (<https://doi.org/10.1073/pnas.2024383118>) using 25 components. The resulting common factor values W were used to calculate similarities between cell types as follows: for each annotated cell type in each dataset, we calculated the mean of

each component from the common factor W; the resulting vectors of mean values of W for each cell type were used to calculate cosine similarity between pairs of cell types.

### Bulk RNA-seq sample preparation and sequencing

To characterize morphogen expressions in the WNT3A node and the DKK1 node, organizer cells were plated into ULA U-bottom 384 well plates as mentioned in the section “Synthetic organizer architecture construction around a mESC core and morphogen induction”. To have 3 replicates of RNA-seq, four plates were prepared for each condition, and each well contained 50 cells. The following day, 200 ng/mL Dox were added to the N2B27 media for the WNT3A node, and 1 uM GRZ were added to the N2B27 media for the DKK1 node. After 2 days, the cells were collected from each well into 1.5 mL tubes. The supernatant was carefully removed, and the samples were frozen at -80°C before extracting RNA.

The RNAs were extracted using Nucleospin RNA plus XS, and all the samples had 20 uL of RNA with a concentration of 50–100 ng/mL. The sequencing and analysis were done by Novogene.

## QUANTIFICATION AND STATISTICAL ANALYSIS

### Statistical analysis

All graphs with error bars report mean  $\pm$  s.e.m. values. For Figures 2E and 4B, Two-tailed unpaired t-tests were performed.

### Quantification of organizer geometries

To quantify the relative degree to which L929 organizer cells arrayed themselves in a single tight node versus a spread-out shell around the mESC embryoid body (Figure S1B), we acquired z-stacks of 5 organizer plus embryoid body assemblies for each condition and took the central slice along the plane that included the largest amount of organizer cells. We then segmented this slice for both mESC cells (far-red channel) and organizer cells (blue channel) with Ilastik and computed the centroid of the mESC body and the relative angular positions of the pixels belonging to the organizer cells around this centroid. The angular distribution of organizer pixels for each condition was then normalized and the similarity to the null distribution of a perfectly even distribution was computed using Jensen-Shannon divergence.

### Analyzing Positions and Morphologies

Imaging data acquired through Opera Phenix microscope were exported as TIFF files and reconstituted as a 4D TIFF file (xyzt) for each color channel, using a custom Python script. Each 3D stack of images was transformed into a 2D maximum projection along the z-axis using the numpy library in Python. To discern cell morphologies, a thresholding technique was applied using the skimage.filter.threshold function. Optimal thresholding methods were evaluated using skimage.filters.try\_all\_threshold prior to final selection. Binary images were generated based on the chosen threshold, from which features characterizing cell morphologies were extracted.

### Measuring relative positions of two nodes on embryoid

The centroids of both embryoid and two nodes were determined utilizing skimage.measure.centroid function. Subsequently, angles between the two nodes were computed based on their positional data in relation to the embryoid (Figure 1E and S1E).

### Quantification of major and minor axis of embryos

Morphological attributes of embryos were quantified using the skimage.measure.regionprops functions, and their elongations were assessed by calculating the ratio of the major axis length to the minor axis length (Figure 3B).

### Plotting reporter signals

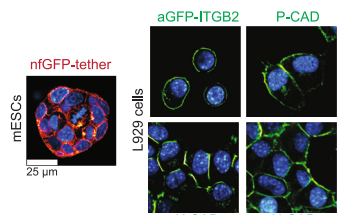
To quantify gradient of reporter signals (Figure 4A, S2A, and S4B), z-slices encompassing the central region of the embryoid were extracted from the 3D TIFF files. Subsequently, a 2D maximum projection along the z axis was generated based on the extracted 3D files. Fluorescence intensity profiles of reporters were assessed in Fiji using a rectangular region of interest (ROI) that encompassed the embryoid.

### Measuring beating cardiac positions in embryoid

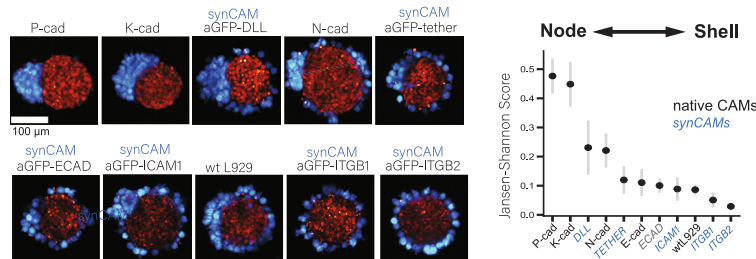
To measure a relative position of beating cardiac region in embryos (Figure 4C), length ( $l$ ) between the WNT3A node and beating domain or cTnT-positive domain were manually measured in Fiji. And this value was then divided by total length ( $L$ ) of the embryoid to calculate the relative position.

# Supplemental figures

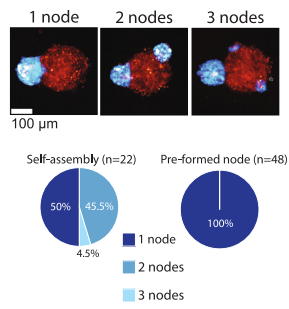
A synCAM/CAM expression on cell surface



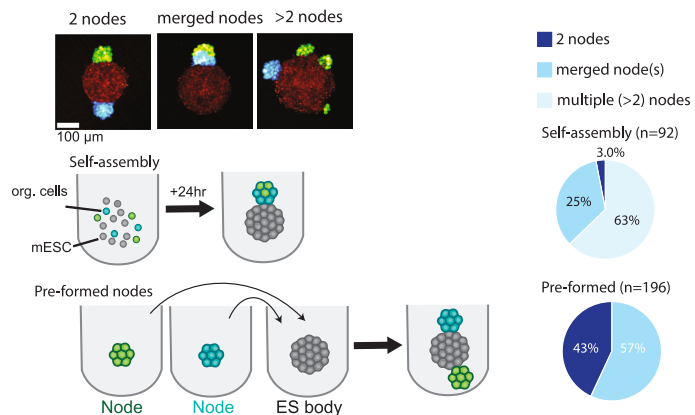
B Distinct sorting of synthetic organizer cells (L929, blue) expressing natural or synthetic adhesion molecules (synCAMs) when interacting with mESCs (red)



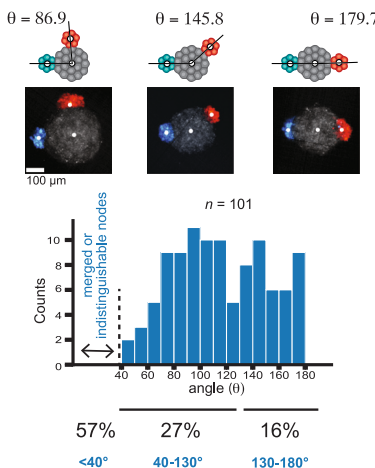
C Probability of forming a single node (organizer: L929 +P-cad +ICAM synCAM)



D Probability of forming two separate nodes



E Histogram of relative position of two nodes (angle)



F Stability of two node relative angular positioning (+/- ICAM1 synCAM)

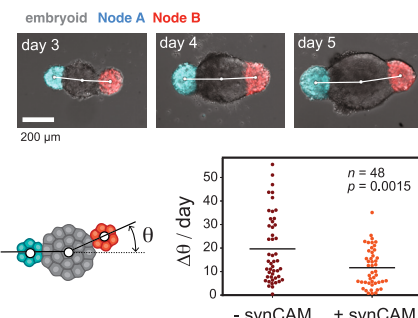


**Figure S1. Construction of diverse synthetic organizer architectures around an embryooid, related to Figure 1**

(A) Immunostaining of adhesion molecules (green or red) to show surface expression of synCAM or native cadherin molecules in mESCs or L929 cells. Nuclei are stained with DAPI. Scale bar: 25 μm.

(legend continued on next page)

(B) Differential sorting of synthetic organizer cells expressing different native or synthetic cell adhesion molecules. Left: representative architectures of synthetic organizer cells (L929, blue) around mESC embryoid (red). Scale bar: 100  $\mu$ m. Right: each architecture was quantified by calculating Jansen-Shannon divergence, which scores the similarity of an architecture to a perfectly even distribution (if the architecture is a complete shell, then the value become 0). Scale bar: 100  $\mu$ m.

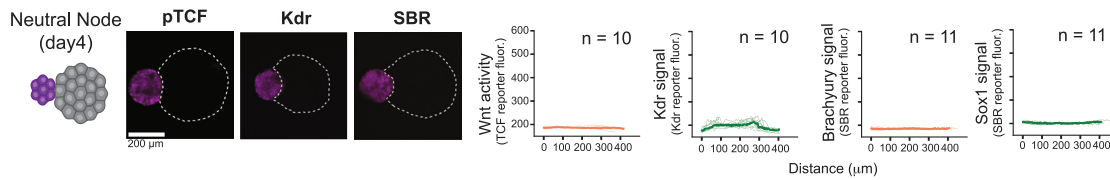
(C) Probability of forming a single vs. multi-node structure. 300 mESCs (red) and 50 synthetic organizer cells (L929 expressing P-cad and Lag16-ICAM1, cyan) were plated together in a well ( $n = 22$ ), and distribution of 1, 2, or 3 node structures (top, representative image) showed self-assembly of approximately equal numbers of 1 and 2 node structures. By contrast, when synthetic organizer cells and mESC were each preformed into spheroids (in separate wells, see Figure 1E), then mixed together, they formed a single-node architecture with 100% reproducibility ( $n = 48$ ). Scale bar: 100  $\mu$ m.

(D) Probability of forming two separate nodes when both organizer cell types (cyan and green, 30 cells each) are plated together with 300 mESCs (red) in a single well (self-assembly,  $n = 92$ ) or preformed in individual wells then combined with an mESC cluster ( $n = 196$ ). Top shows representative images. Scale bar: 100  $\mu$ m.

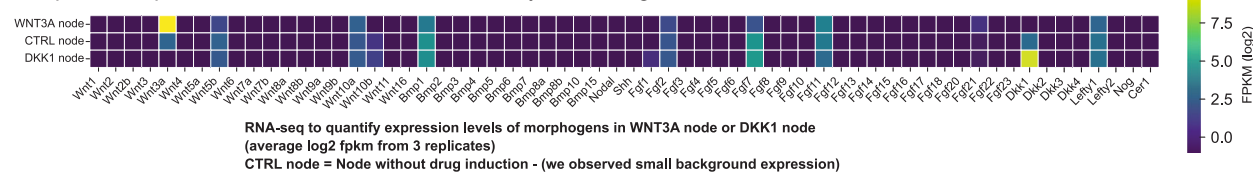
(E) Histogram of relative angular positions of two node structures where nodes are preformed ( $n = 196$ ). 57% of structures result in merged or indistinguishable nodes (angle < 40°). In the remaining 101 structures, 27% have a relative angle of 40°–130°, and 16% have a relative angle of 130°–180° (approx. opposite each other). Our detailed analysis in this study focused on dual-node structures with a relative angle of 130°–180°. Scale bar: 100  $\mu$ m.

(F) Stability of two-node relative angular positioning. Top: days 3–5 representative images showing the stable relative orientation of two distinct nodes (blue/red) around an mESC cluster (gray). White circles indicate centroids of the embryoid and the nodes. Bottom: distribution of relative angular change in two-node structure per day, comparing nodes that do and do not express anti-GFP synCAM (Lag16-ICAM1).  $\Delta\theta$  indicates change in angle per day, and horizontal bars in the plots are the mean value of  $\Delta\theta$ . \* $p < 0.05$ , unpaired  $t$  test. We find that the addition of synCAM interaction between nodes and mESCs leads to reduced angular change. Scale bar: 200  $\mu$ m.

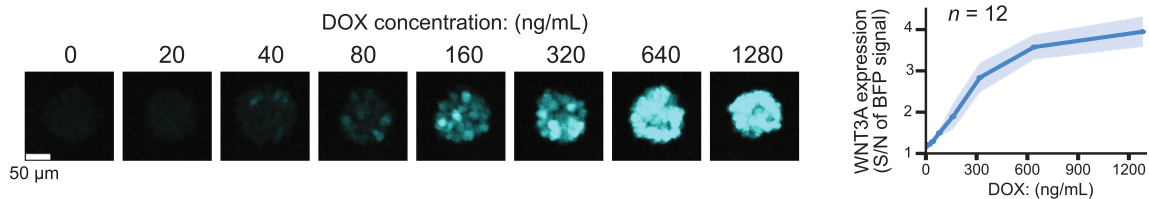
A No reporter activation without WNT3A production



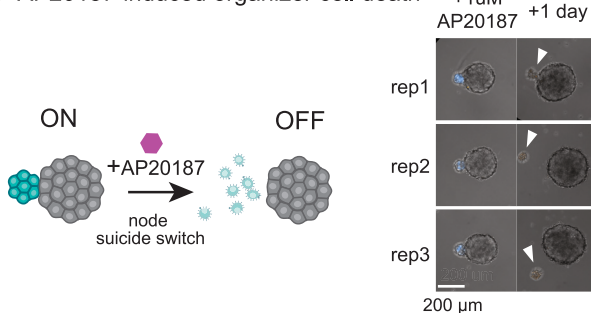
B Specific expression of WNT3A or DKK1 from synthetic organizers



C Dox induced control of WNT3A-IRES-BFP node



D AP20187-induced organizer cell death



E Robustness to Wnt node size variation

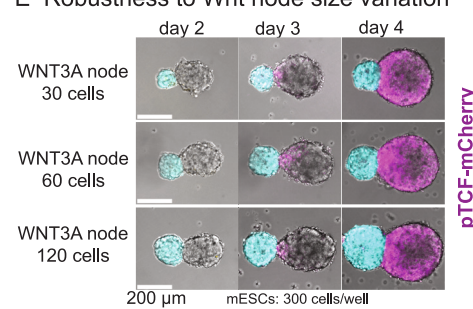
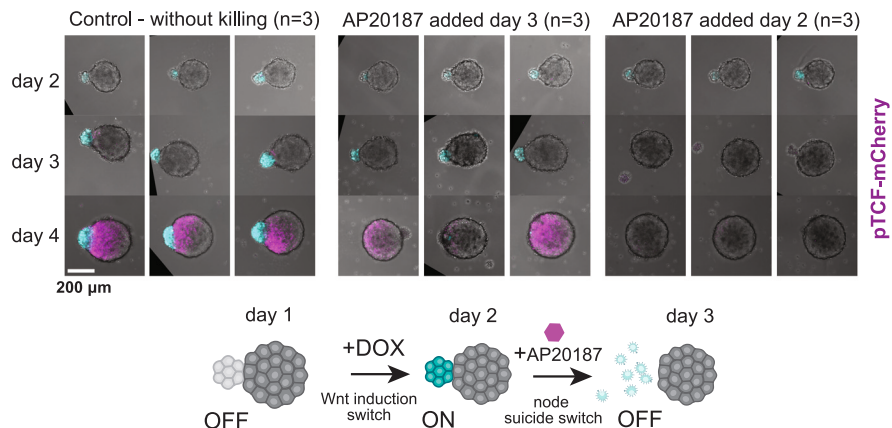


**Figure S2. Analysis of the WNT3A node synthetic organizer, related to Figure 2**

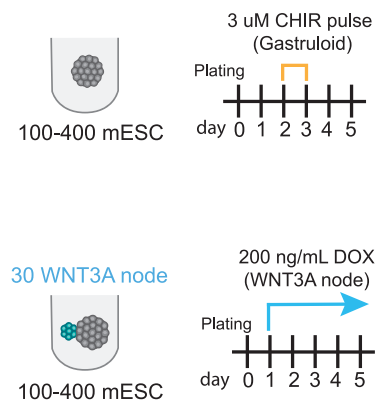
- (A) pTCF-mCherry, Kdr, or Sox1/Brachury (SBR) reporter activity in mESC embryoids with a neutral node (lacking Wnt secretion). Representative images and fluorescence intensity profiles are shown. The bold line shows the median of individual profiles ( $n = 10\text{--}11$  per reporter). Scale bar: 200  $\mu\text{m}$ . No evidence for signaling to the mESCs from the neutral node is observed.
- (B) Bulk RNA-seq analysis of WNT3A or DKK1 nodes 2 days after induction with 200 ng/mL DOX or 1  $\mu\text{M}$  GRZ, respectively, vs. CTRL nodes (no drug induction or morphogen production) to quantify the expression levels of morphogens basally expressed by L929 organizer cells.
- (C) Amplitude control of WNT3A-IRES-BFP production by synthetic organizer cells by titrating the concentration of DOX. Left: representative images and intensity profiles of BFP fluorescence with different WNT3A node induction levels. Scale bar: 50  $\mu\text{m}$ . Right: quantification of BFP signal intensity with varying DOX concentration ( $n = 12$ ).
- (D) Suicide switch induced by AP20187 in synthetic node organizer cells. Left: schematic diagram of suicide switch induction by 1.0  $\mu\text{M}$  AP20187 treatment. Right: representative images from 3 replicates showing apoptosis and detachment of node cells (white arrows) within 1 day of treatment. Scale bar: 200  $\mu\text{m}$ .
- (E) pTCF-mCherry reporter activity (purple) in embryoids seeded from 300 mESC and combined with a WNT3A node (cyan) seeded from 30, 60, or 120 cells with 200 ng/mL DOX after day 1. Scale bar: 200  $\mu\text{m}$ . The establishment of WNT activity gradient is robust to this variation in number of organizer cells.

A induced cell-death of WNT3A node shows that node signaling is required for 3+ days to generate pTCF gradient

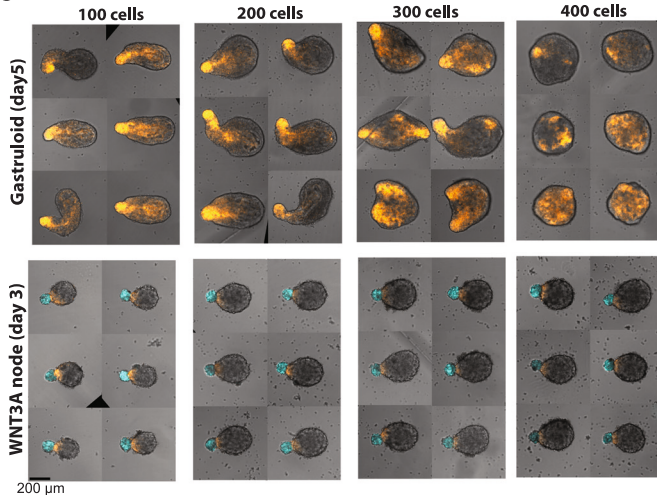


Sensitivity of symmetry breaking to the initial number of mESCs

B



C



D DKK1 node + CHIR pulse yields robust directed polarization

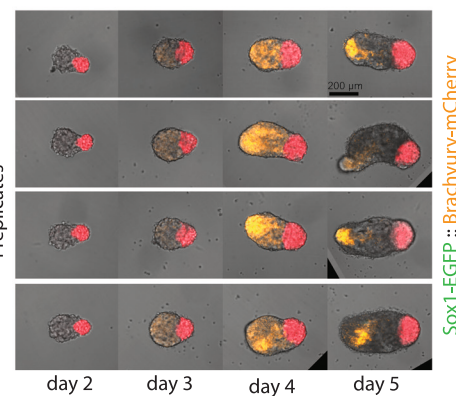
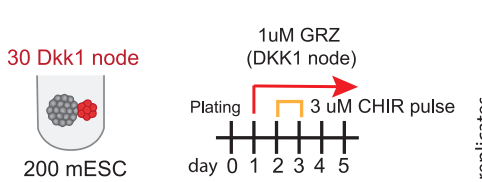


**Figure S3. Analysis of alternative mechanisms to induce embryoid polarization, related to Figure 2**

(A) Effect of induced cell death of WNT3A node at different times on pTCF-mCherry reporter activity (purple). Bottom: schematic diagram of experimental conditions, with induction of WNT3A production using 200 ng/mL DOX on day 1, followed by suicide switch induction using 1  $\mu$ M AP20187. Top: effect of killing the node (cyan) on Wnt gradient formation (pTCF-mCherry reporter, purple). Inducing the suicide switch on day 3 (middle) leads to WNT activity without a clear gradient, while inducing the suicide switch on day 3 (right) prevents any significant induction of WNT activity. Scale bar: 200  $\mu$ m.

(legend continued on next page)

---

(B) Schematic diagram of experimental conditions for the gastruloid protocol (3  $\mu$ M CHIR pulse between days 2 and 3) vs. the WNT node protocol, where WNT3a production is induced on day 1 by adding 200 ng/mL DOX.

(C) Sensitivity of symmetry breaking to the initial number of mESCs using either the gastruloid protocol or the WNT node protocol. WNT3a nodes are shown in cyan, Brachyury-mCherry reporter activity is shown in orange. Six individual replicates are shown per condition, 72 h after induction of WNT signal (day 5 for gastruloids, day 3 for WNT node protocol). Scale bar: 200  $\mu$ m. For gastruloid protocol, 3  $\mu$ M CHIR pulse is given between days 2 and 3. For the WNT node protocol, WNT3a production is induced on day 1 by adding 200 ng/mL DOX.

(D) Combining a CHIR pulse with a DKK1 node yields robust and directed polarization of the embryoids. Left: schematic diagram of experimental conditions. DKK1 node is induced continuously from day 1, followed by a 3  $\mu$ M CHIR pulse between days 2 and 3. Right: polarization of Brachyury-mCherry reporter activity (orange) away from the DKK1 node (red) is observed between days 2 and 5 in 4 individual replicates. Scale bar: 200  $\mu$ m.

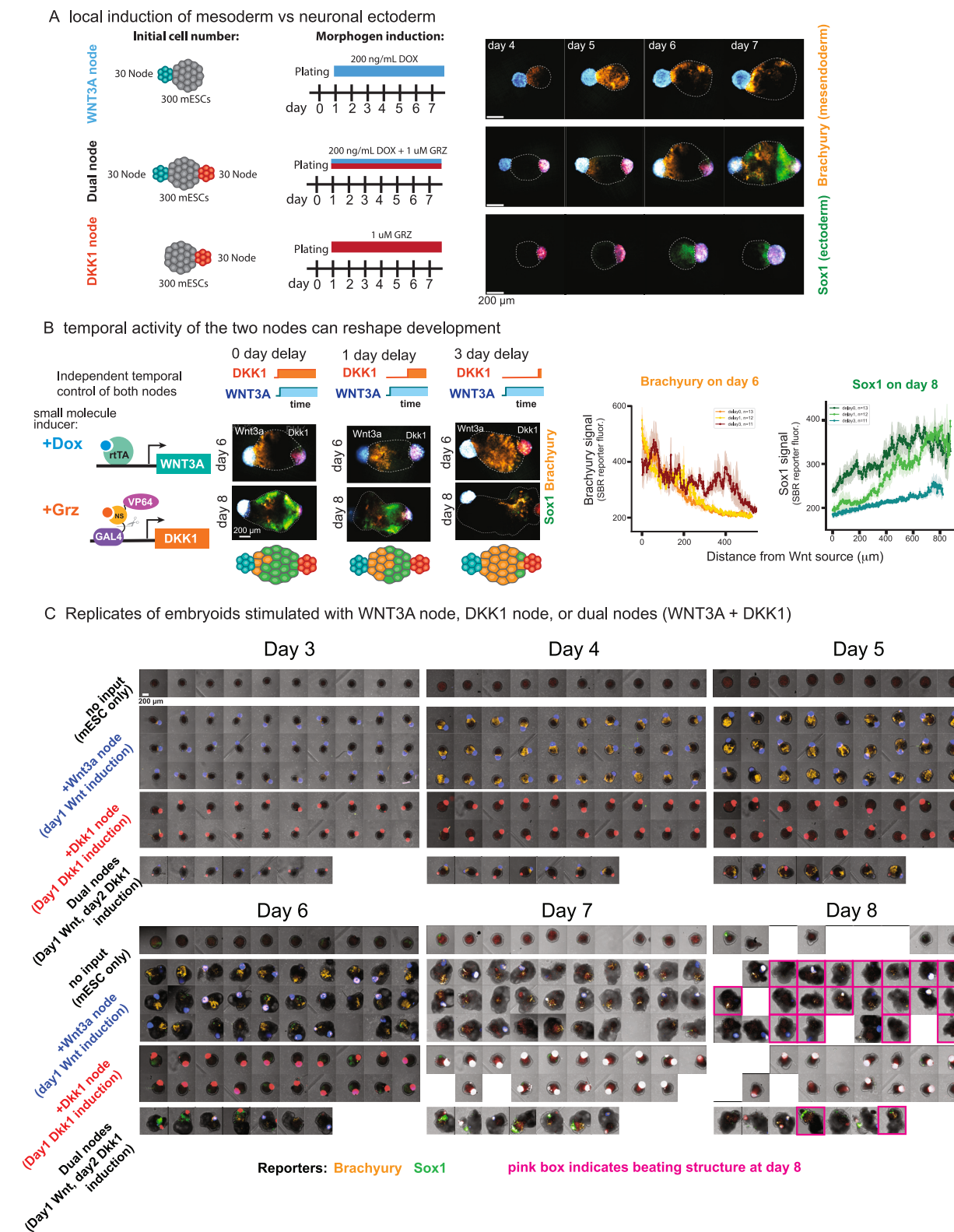


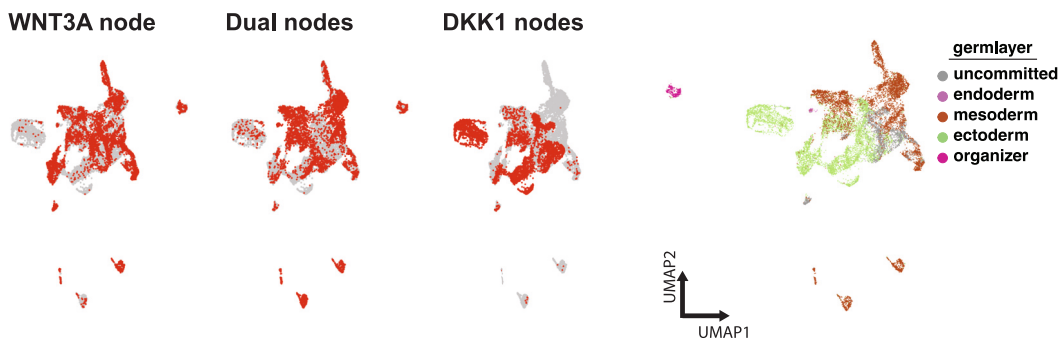
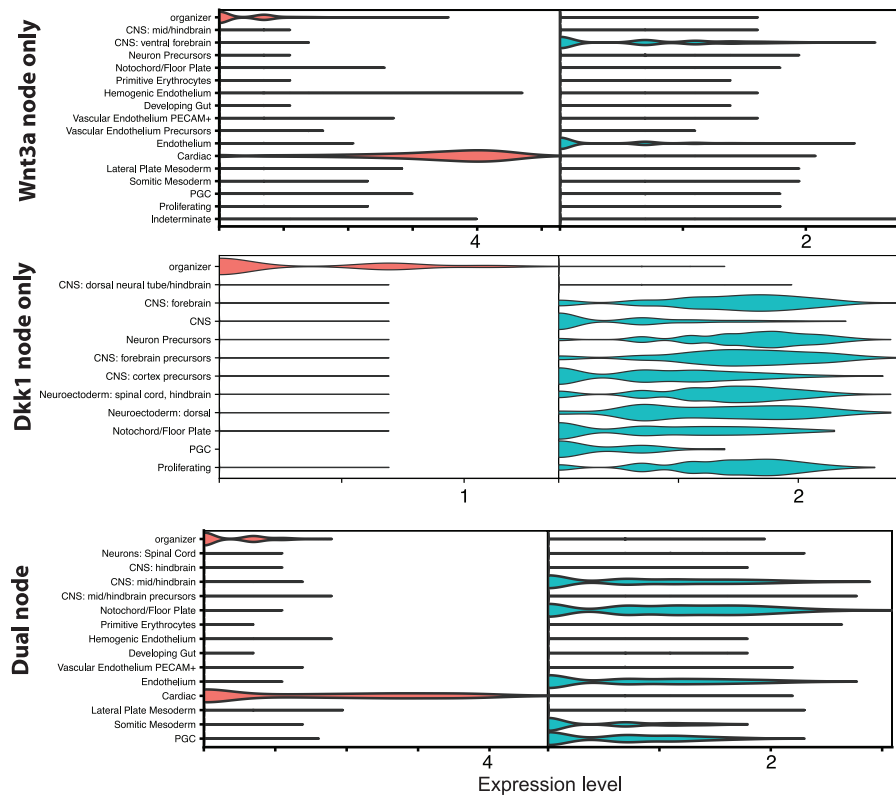
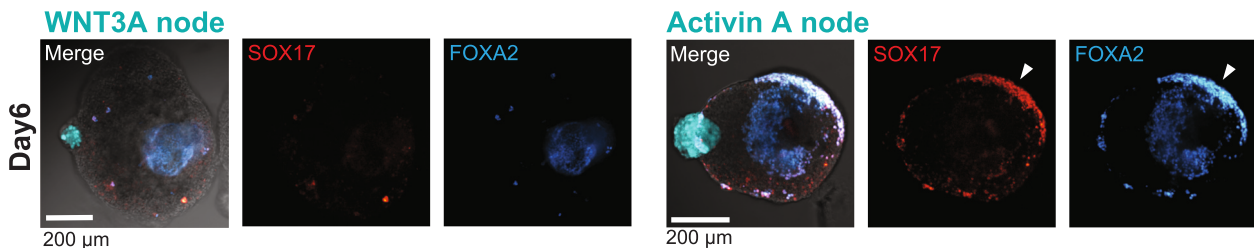
**Figure S4. Additional analysis of WNT3A/DKK1 dual-node organizer outcomes, related to Figure 3**

(A) Synthetic organizers induce local cellular patterning. Left: schematic diagram of experimental conditions using single WNT3A node induced by 200 ng/mL DOX starting day 1, single DKK1 node induced by 1 μM GRZ starting day 1, or dual nodes co-induced starting on day 1. Right: live-cell imaging of

(legend continued on next page)

Brachyury-mCherry (orange)::Sox1-EGFP (green) reporter mESCs showed that the WNT3A node primarily induced Brachyury expression, whereas DKK1 node primarily induced Sox1 expression. Opposing WNT3A and DKK1 nodes (dual nodes) induced Brachyury close to WNT source and Sox1 close to DKK1 source. Scale bar: 200  $\mu$ m.

(B) Optimization of relative timing of WNT3A and DKK1 induction. Left: WNT3A and DKK1 nodes use different chemical inducer systems to produce their payload: DOX for WNT3A and GRZ for DKK1. Middle: with no delay, distribution of Sox1-positive cells is dominant by day 8. Delaying DKK1 induction by 1 day results in more balanced distribution of Brachyury- and Sox1-positive cells. Delaying DKK1 by 3 days leads to a dominant distribution of Brachyury-positive cells. Scale bar: 200  $\mu$ m. Right: quantification of Brachyury distribution on day 6 and Sox1 distribution on day 8 in embryoids ( $n = 11\text{--}13$  per condition). Scale bar: 200  $\mu$ m.  
(C) Replicates of mESCs with WNT3A node (blue), DKK1 node (red), or dual nodes (WNT3A + DKK1) where the two nodes are separated by 130°–180°. Time course of embryoids (Brachyury-mCherry (orange)::Sox1-EGFP (green) reporter line) between days 3 and 8. Pink box indicates beating on day 8. Missing embryoids were damaged during media changes. Both the WNT3A node and the dual-node contexts lead to consistently greater embryoid growth and elongation, in addition to the regionalized beating phenotype. Scale bar: 200  $\mu$ m.

**A UMAP colored by organizer and germlayer type****B Violin plots of *TnnT2* (cardiac marker) and *Tubb3* (neural marker) in each condition****C Activin A node induction yields higher level of definitive endoderm (Double positive of SOX17 and FOXA2)**

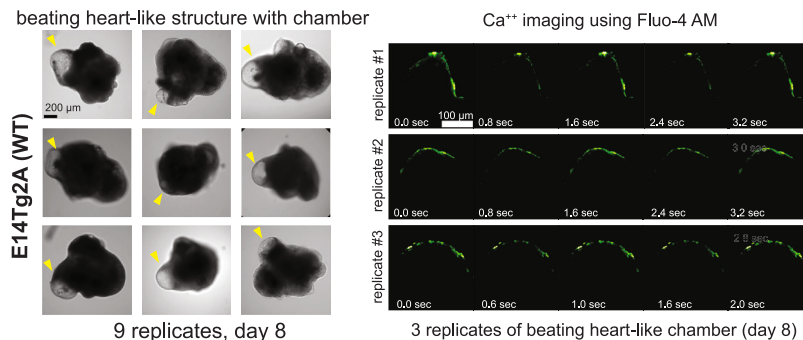
**Figure S5. Comparison of resulting germline lineages generated by the different organizer structures, related to Figure 4**  
 (A) UMAP visualization of cells from the different organizer structures (left) and the germline types from which the cells are derived (right). This analysis shows how the WNT3A node organizer largely generates mesoderm lineages, the DKK1 node organizer exclusively generates ectoderm lineages, and the dual-node organizer generates a distribution of mesoderm and ectoderm lineages.

(legend continued on next page)

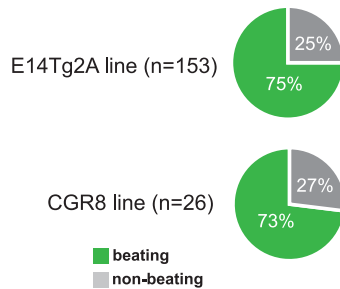
---

(B) Violin plots showing *Tnnt2* (cardiac troponin T gene; encodes cTnT2 protein) and *Tubb3* (neural  $\beta$ -tubulin) expression in each embryoid type (WNT3A single node, DKK1 single node, and dual node).  
(C) Synthetic organizer node producing Activin A (cyan, right) favors definitive endoderm formation (left), marked by co-expression of SOX17 (red) and FOXA2 (cyan). By contrast, WNT3A node (cyan, left) yields limited definitive endoderm. Imaging in both cases is performed on day 6. Scale bar: 200  $\mu$ m.

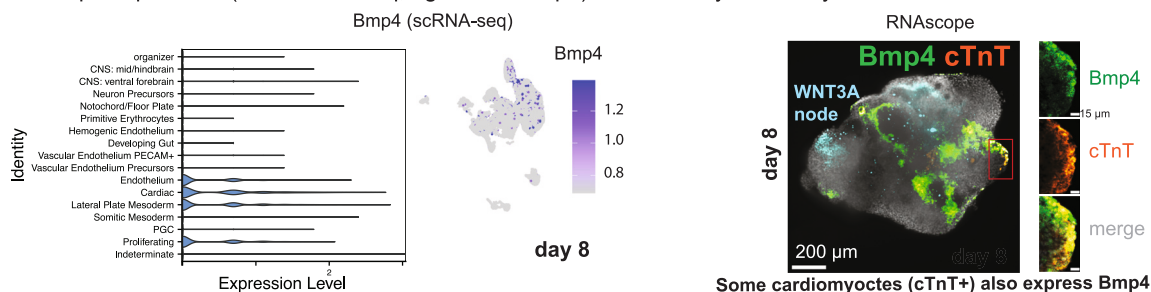
**A Replicates of beating heart structure that emerges from Wnt3a single node induction**



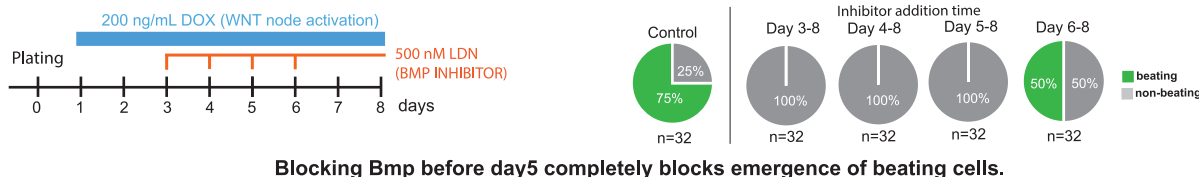
**B Diverse mESC lines yield beating heart when treated with WNT3A node**



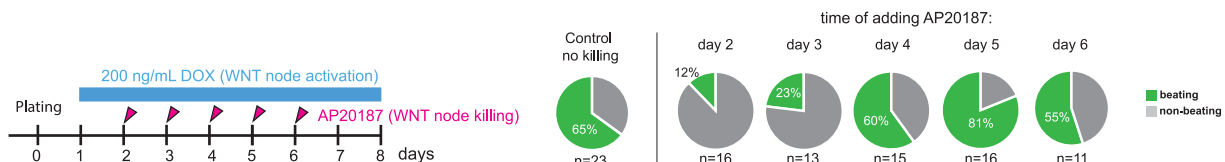
**C Bmp4 expression (left: scRNA-seq, right: RNAscope) inside embryo on day 8**



**D Add LDN193189 (BMP inhibitor) at different time points**



**E Use suicide switch to analyze duration of WNT3A node signaling required for induction of beating cardiac structure**



At least 3-4 days of WNT3A node signaling is required to generate beating cardiac structure

**Figure S6. Characterization of beating cardiac structures, related to Figure 6**

(A) Replicates: formation of beating, chambered, heart-like structure that emerges from WNT3A single-node induction, related to Figures 6C and 6F. Left: 9 representative images of a beating chamber on day 8. Yellow arrowhead indicates a beating chamber. Scale bar: 200 µm. Right: 3 replicates of live recording beating heart-like chamber using Fluo-4 AM. Scale bar: 100 µm.

(B) Quantification of beating heart-like phenotype in WNT3A node structures from two distinct mESC lines on day 8: 75% of embryos from E14Tg2A line developed beating domains ( $n = 153$ ), and 73% of embryos from CGR8 line developed beating domains ( $n = 26$ ).

(C) Bmp4 expression in WNT3A node-induced embryo on day 8. Left: violin plot of Bmp4 expression in cell populations from WNT3A organizer embryos. Middle: feature plot showing the distribution of Bmp4-expressing cells on the UMAP of WNT3A organizer embryos. Right: representative Bmp4 RNAscope (green) and cTnT staining (red) far from WNT3A node (cyan). Scale bar: 200 µm. Inset: Bmp4 and cTnT signals are co-localized in heart-like domain. Inset scale: 15 µm.

(legend continued on next page)

- 
- (D) Effect of blocking BMP signaling on beating domain formation. Left: schematic diagram of experimental conditions, with WNT3A node induced by DOX starting day 1, followed by the addition of 500 nM of LDN193189 (BMP inhibitor) starting days 3, 4, 5, or 6. Right: quantification of beating domain formation ( $n = 32$  embryos per condition). Inhibiting BMP signaling before day 5 completely blocks the emergence of beating domains, while blocking BMP signaling on day 6 reduces the proportion of embryos that develop a beating domain.
- (E) Effect of killing WNT3A node cells on beating cardiac domain development. Left: schematic diagram of experimental conditions, with WNT3A node induced by DOX starting day 1, followed by induction of the suicide switch by addition of 1  $\mu$ M AP20187 on days 2–6. Right: quantification of beating domain formation ( $n = 11$ –23 embryos per condition). Killing WNT3a-producing node cells on days 2 or 3 reduces the efficiency of beating domain formation, while killing on or after day 4 or later has little effect.